



HAL
open science

Impact-induced chemical fractionation as inferred from hypervelocity impact experiments with silicate projectiles and metallic targets

Clément Ganino, Guy Libourel, Akiko Nakamura, Suzanne Jacomet, Olivier Tottereau, Patrick Michel

► To cite this version:

Clément Ganino, Guy Libourel, Akiko Nakamura, Suzanne Jacomet, Olivier Tottereau, et al.. Impact-induced chemical fractionation as inferred from hypervelocity impact experiments with silicate projectiles and metallic targets. *Meteoritics and Planetary Science*, 2018, 53 (11), pp.2306-2326. 10.1111/maps.13131 . hal-02196123

HAL Id: hal-02196123

<https://hal.science/hal-02196123v1>

Submitted on 11 Dec 2024


HAL is a multi-disciplinary open access archive for the deposit and dissemination of scientific research documents, whether they are published or not. The documents may come from teaching and research institutions in France or abroad, or from public or private research centers.

L'archive ouverte pluridisciplinaire **HAL**, est destinée au dépôt et à la diffusion de documents scientifiques de niveau recherche, publiés ou non, émanant des établissements d'enseignement et de recherche français ou étrangers, des laboratoires publics ou privés.



Distributed under a Creative Commons Attribution 4.0 International License

Impact-induced chemical fractionation as inferred from hypervelocity impact experiments with silicate projectiles and metallic targets

Clément GANINO ^{1*}, Guy LIBOUREL^{2,3}, Akiko M. NAKAMURA⁴, Suzanne JACOMET⁵, Olivier TOTTEREAU⁶, and Patrick MICHEL²

¹Université Côte d'Azur, OCA, CNRS, Géoazur, 250 rue Albert Einstein, Sophia-Antipolis, 06560 Valbonne, France

²Université Côte d'Azur, OCA, CNRS, Lagrange, Boulevard de l'Observatoire, CS 34229, 06304 Nice Cedex 4, France

³Hawai'i Institute of Geophysics and Planetology, School of Ocean, Earth Science and Technology, University of Hawai'i at Mānoa, Honolulu, Hawai'i 96821, USA

⁴Graduate School of Science, Kobe University, 1-1 Rokkoudai-cho, Nada-ku, Kobe 657-8501, Japan

⁵MINES ParisTech, PSL—Research University, CEMEF—Centre de mise en forme des matériaux, CNRS, UMR 7635, Sophia-Antipolis, France

⁶CRHEA, CNRS UPR 10, Sophia Antipolis, France

*Corresponding author. E-mail: ganino@unice.fr

(Received 08 June 2017; revision accepted 07 May 2018)

Abstract—Hypervelocity impacts are common in the solar system, in particular during its early phases when primitive bodies of contrasted composition collided. Whether these objects are chemically modified during the impact process, and by what kind of processes, e.g., chemical mixing or gas–liquid–solid fractionation, are still pending questions. To address these issues, a set of impact experiments involving a multielemental doped phonolitic projectile and a metallic target was performed in a 3–7 km s^{−1} range of impact speeds which are typical of those occurring in the asteroid belt. For each run, both texture and chemistry of the crater and the ejecta population have been characterized. The results show that the melted projectiles largely cover the craters at all speeds, and that melted phonolitic materials are injected into fractures in the crater in the metallic target. Ejecta are generally quenched droplets of silicate impact melt containing metal beads. Some of these beads are extracted from the target, but we propose that some of the Fe metal beads are the result of reduction of FeO. A thin FeO–SiO₂-rich condensate layer is found at the edge of the crater, suggesting that a limited amount of vapor formed and condensed. LA-ICP-MS analyses suggest, however, that within analytical uncertainties, no volatility-controlled chemical fractionation of trace elements occurred in the ejecta. The main chemical fractionation during impact at such velocities and energies are the result of projectile–target mixing.

INTRODUCTION

Impact cratering is considered to be one of the most important geological processes in the history of our planetary system (Melosh 1989; French 1998). Impact craters are indeed omnipresent on the surfaces of both asteroids and planetary bodies. They result from collisions between two bodies at speeds in excess of a few km s^{−1}. Typical impact velocities depend on the location in the solar system, along with the precise details of the relative orbits of the respective bodies and

their mutual gravitational influence. While impacts are distributed over a wide range of speeds in the solar system (Le Feuvre and Wieczorek 2011), most impact speeds are in the range of 1–30 km s^{−1} for the inner solar system. For instance, mean collision speeds in the asteroid belt are about 5 km s^{−1} (Bottke et al. 1994), falling to around 1 km s^{−1} in the vicinity of Pluto (Greenstreet et al. 2015). For the Earth–Moon system, average velocities are much higher, between 15 and 25 km s^{−1} (Oberst et al. 2012). Typical impact speeds also depend on the stage of the solar system evolution

at which impacts occurred, i.e., during protoplanetary disk, debris disk, planet migration phases, or now. Very likely, the so-called “Grand Tack” scenario (Walsh et al. 2011), in which Jupiter temporarily entered the asteroid belt region before migrating back outward, might have resulted in collisions at higher velocities than during the current era.

High-speed impacts have been widely studied for their role in catastrophic disruptions, concentrating mainly on their outcome on the target. The interaction between target and projectile during natural impact events and experimental hypervelocity impacts, on the other hand, has rarely been studied (Kelly et al. 1974; Gibbons et al. 1976; Horz et al. 1989; Evans et al. 1992; Mittlefehldt et al. 1992, 2005; Ebert et al. 2011, 2013, 2014; Wozniakiewicz et al. 2011; Hamann et al. 2013, 2016a, 2017). This is in part due to the complexity of such kind of experimental studies, and also linked to the fact that during large impact events, the projectile is melted or vaporized so that, at best, only small fragments survive (e.g., Mittlefehldt et al. 1992).

On the other hand, it is reasonable to expect that, in the frame of highly energetic, violent, and ultrafast impact events, phase transformations accompanied by various chemical fractionation processes (e.g., induced during melting and subsequent quenching, or evaporation and subsequent condensation, etc.) can occur as pressure and temperature reach extreme values. An example is the gas-associated spheroidal precipitates described in lunar regolith breccia 14076 (Warren 2008) compositions highly depleted in refractory oxides (Al_2O_3 and CaO) and which are interpreted as resulting from condensation from an impact vapor plume. Nevertheless, kinetically, the time scale of an impact is of the order of seconds or less, which might constitute a strong limitation in the completion of chemical fractionation from melting/evaporation and other classical magmatic processes known from Earth and other planetary bodies that are closer to equilibrium conditions.

Laboratory experiments and theoretical models have demonstrated that collisions can lead to different types of sticking, bouncing, and fragmentation (e.g., Güttler et al. 2010; Jutzi et al. 2015) depending on impact speed, porosity, and on the relative size of the involved bodies. In most of these processes, a mass transfer and a degree of mixing (as solid fragments and as impact melts derived from projectile and target) is expected. However, previous studies suggest that the process of projectile–target mixing and the formation of impactite is very complex and far from being understood (Evans et al. 1992; Mittlefehldt et al. 1992, 2005; Wozniakiewicz et al. 2011; Koeberl et al. 2012; Ebert et al. 2013, 2014; Hamann et al. 2013, 2016b).

Element fractionation during impact melting is, for instance, documented in impact melts from the Wabar crater where a complex vapor fractionation process produced siderophile element abundances in the impact melts that differ from those of the projectile (Mittlefehldt et al. 1992). On the other hand, siderophile element ratios in the impact melts from Meteor Crater are mostly unchanged from those of the projectile, although depletion in Au has been ascribed to loss of volatile Au halides (Mittlefehldt et al. 2005). Aside from these studies, several experimental studies have focused on impact-induced element fractionation processes. Ebert et al. (2013, 2014) described physical and chemical mixing of sandstone-derived impact melts with metallic impact melts derived from projectiles made of steel or the Campo del Cielo iron meteorite. Specifically, Ebert et al. (2013, 2014) described significant interelement fractionation, i.e., selective enrichment of Fe in the silicate melt, and enrichment of Ni and Co in coexisting projectile melt spherules. In addition, Ebert et al. (2014) observed that Cr (and V) of the projectile droplets preferentially partitioned into the silicate melt with respect to Fe, yielding Cr/Fe well above the target and projectile ratios. Hamann et al. (2013) focused on the impact glass from the Wabar crater, Saudi Arabia and demonstrated that meteoritic Fe was selectively mixed with high-silica target melt at high temperatures due to selective oxidation. Subsequent fractionation occurred during quenching of the melt by unmixing due to liquid immiscibility separating iron-rich and silica-rich melts. Rowan and Ahrens (1994) focused on basalt–molybdenum interactions during shock experiments and described the in situ reduction of FeO in the shocked melted basalt. Hamann et al. (2016a, 2016b) investigated the chemical interaction between Cu-bearing aluminum projectiles and quartz sand targets in hypervelocity impact experiments and redox reactions between Cu-bearing Al alloy and SiO_2 (forming Al_2O_3 melt and silicon as euhedral crystals, or spherical droplets).

These results illustrate that chemical fractionation processes, at least associated to redox reaction, occur during the short time scales of an impact and are various and complex. However, bridging the gap between impact experiments and natural observations is challenging because the impact energies are extremely different: the maximum impact velocities currently obtained for macroscopic (mm-sized) projectiles in the laboratory are limited to 6–8 km s^{-1} , resulting in low impact energy. Thus, impact energies in experiments are typically in the 10^{-1} to 10^2 J range (Ebert et al. 2014), whereas those calculated for small natural craters such as Wabar or Meteor Crater are about 10^7 kJ (Melosh and Collins 2005). Laser heating experiments (Hamann

et al. 2016a, 2016b; Ebert et al. 2017) produce superheated melts that thermodynamically, texturally, and mineralogically resemble impact melts formed during adiabatic decompression. Such experiments may extend attainable temperatures in experiments to ranges corresponding to impacts in the velocity range of 4–20 km s⁻¹, and may contribute to the study of time scales and magnitudes of petrogenetic processes in impact melts. A limitation is the absence of high shock pressures in these experiments, which remain complementary to hypervelocity experiments.

In the previous hypervelocity experiments mentioned above, chemical fractionation during melting and mixing of projectile and target material was only described for a limited number of chemical components. Consequently, the aim of this study was thus to extend the investigation of interelement fractionation to a larger set of chemical components that range from refractory to siderophile to highly volatile elements, and to explore chemical fractionation associated with impacts at speeds typical of those occurring in the asteroid belt (some 5 km s⁻¹). In order to test unambiguously the occurrence of any chemical fractionations while remaining close to the context of solar system collisions and respecting the experimental constraints, our strategy has been to perform impact experiments by shooting a projectile made of trace element-doped phonolitic (Table 1) glass beads onto a steel (Table 2) target. The phonolitic glass is used as a proxy of silicate material that is the major composition of most undifferentiated meteorite. Fifteen elements, representing a large spectrum of different chemical affinities from refractory to siderophile and to highly volatile elements, have been added to the phonolite composition (Table 1) to facilitate the recognition of any chemical fractionation. For each experiment, both the crater and the ejecta—the latter recovered using aluminum witness plates—have been characterized by scanning electron microscopy (SEM) techniques and analyzed by energy dispersive spectroscopy (EDX) and laser ablation–inductively coupled plasma–mass spectrometry (LA-ICP-MS).

EXPERIMENTS AND ANALYTICAL TECHNIQUES

Experiments

The projectile composition (Table 1) has been selected to be close to that of a phonolitic lava (55–60 wt% SiO₂ and ~15 wt% Na₂O+K₂O), a composition that maximizes the alkali (volatile) element contents. Crystal-free natural phonolitic glassy chips were ground in a mortar to a fine powder at CRPG-SARM Nancy. Fifteen trace elements (Ba, Ce, Cs, Co, Ga, La, Nb, Rb, Sc, Sr,

Table 1. ICP-MS analyses of the bulk composition (wt%) of the phonolitic projectile.

	Bulk projectile (<i>n</i> = 4)	2σ
SiO ₂	57.5	1.1
Al ₂ O ₃	13.8	0.3
Fe ₂ O ₃	4.06	0.20
MnO	0.11	0.00
MgO	4.52	0.07
CaO	4.62	0.09
Na ₂ O	6.03	0.30
K ₂ O	7.92	0.11
TiO ₂	1.11	0.02
Total	99.63	1.4
Ba	900	14
Ce	824	28
Co	641	83
Cs	737	23
Ga	322	49
La	745	5
Nb	685	7
Rb	839	19
Sc	342	4
Sr	753	12
Ta	983	25
V	569	16
Y	850	6
Yb	842	28
Zr	670	4

L.D. = limit of detection.

Table 2. Nominal composition (wt%) of the steel from the target and the aluminum ejecta catcher.

	Target	Ejecta catchers
Si	0.15–0.35	0.14–0.25
Al		98.32–98.35
Fe		0.09–0.1
Mn	0.6–0.9	0.04–0.06
Mg		0.74–0.75
Ca		0.03
Na		0.39–0.49
K		0.07
Ti		0.04–0.05
P	<0.03	
C	0.33–0.38	
S	<0.03	
Cu	<0.3	
Ni	<0.25	
Cr	0.9–1.2	
Mo	0.15–0.3	

Ta, V, Y, Yb, and Zr) ranging in concentrations from 300 to 1000 ppm were then added as oxides to this powder. The obtained mixture was then homogenized, and remelted 5 min at 1400 °C in a Gero muffle furnace using

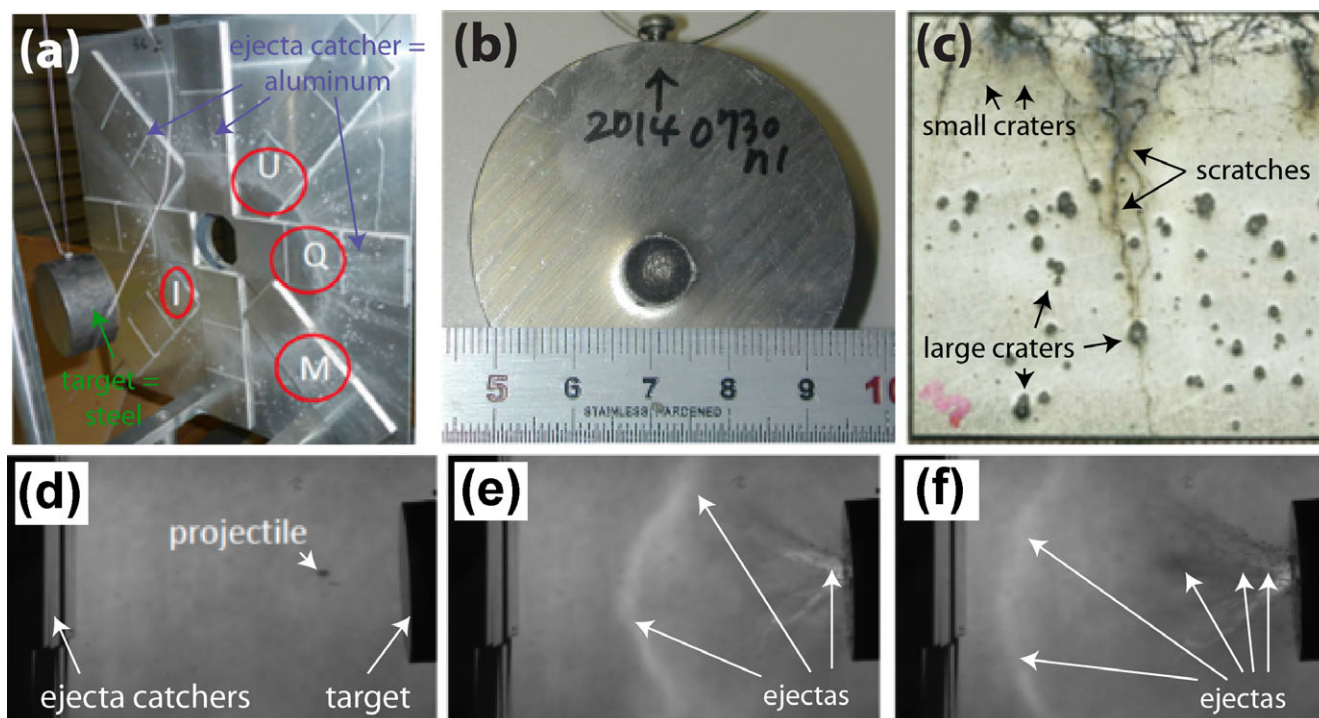


Fig. 1. a) Experimental setup; (b) steel cylinder used as target with the resulting impact crater (here after impact from experiment n1); (c) aluminum ejecta catcher with macroscopic craters and scratches (scars) (1 cm × 1 cm); (d–f) high-speed video camera images of the impact during experiment n0 (d) after the shoot, (e) 12 μs after impact, and (f) 16 μs after impact. (Color figure can be viewed at wileyonlinelibrary.com.)

amorphous carbon crucible for making, after quenching ($\sim 100\text{ }^\circ\text{C s}^{-1}$), a dozen 2–5 mm homogeneous glassy spherical beads (Fig. S1 in supporting information). Four of them were selected to define the bulk chemical composition of the starting material (Table 1; see below), and the remaining ones were used as projectiles for the set of hypervelocity impact experiments described here. The targets consist in a SCM 435 steel cylinder of 5–6 cm radius and 3–4 cm height; minor element abundances, as provided by the supplier, are given in Table 2. Ejecta were collected on witness made of aluminum (Fig. 1; composition as provided by the supplier is given in Table 2), allowing convenient detection of silica- and/or iron-rich ejecta.

The impact experiments were performed using a 7 mm bore two-stage light-gas gun at the Institute of Space and Astronautical Science (ISAS) in Japan. Projectiles were all shot vertically to the target surface using a plastic sabot (Kawai et al. 2010). The range of impact speeds is between 3 and 7 km s^{-1} , allowing the determination of the scaling of the results with impact speed (see Table 3). A square aluminum witness plate (28 cm width) with a central hole (4 cm in diameter) allowing the passage of the projectile was placed in front of the target. Smaller aluminum plates (1 cm width) were fixed on the large aluminum witness plate and were

Table 3. Experimental setup.

Exp. number	Impact velocity (km s^{-1})	Mass of the projectile (g)	Energy (J)
n3	3.39	0.033	190
n1	4.9	0.037	444
n4	6.88	0.03	710
n0	6.89	0.08	1899

used for the analyses. The distance between the witness plate that collected the ejecta and the target surface was about 10 cm (see Fig. 1). All the experiments were performed under vacuum condition ($<10\text{ Pa}$).

A total of five experiments were performed with increasing impact speed (from 3.39 to 6.89 km s^{-1}) and different projectile mass (from 0.03 to 0.08 g), resulting in impact energies that ranged from 190 to 1899 J (see Table 3). The trajectories of the projectile and the ejecta were captured with a high-speed video camera (frame rate of 4 μs) that monitored the experiments.

Scanning Electron Microscopy

Backscattered electron (BSE) imaging of the resulting craters (Fig. 2) and ejecta (Fig. 3) as well as major element analysis was done using a Philips FEI XL30

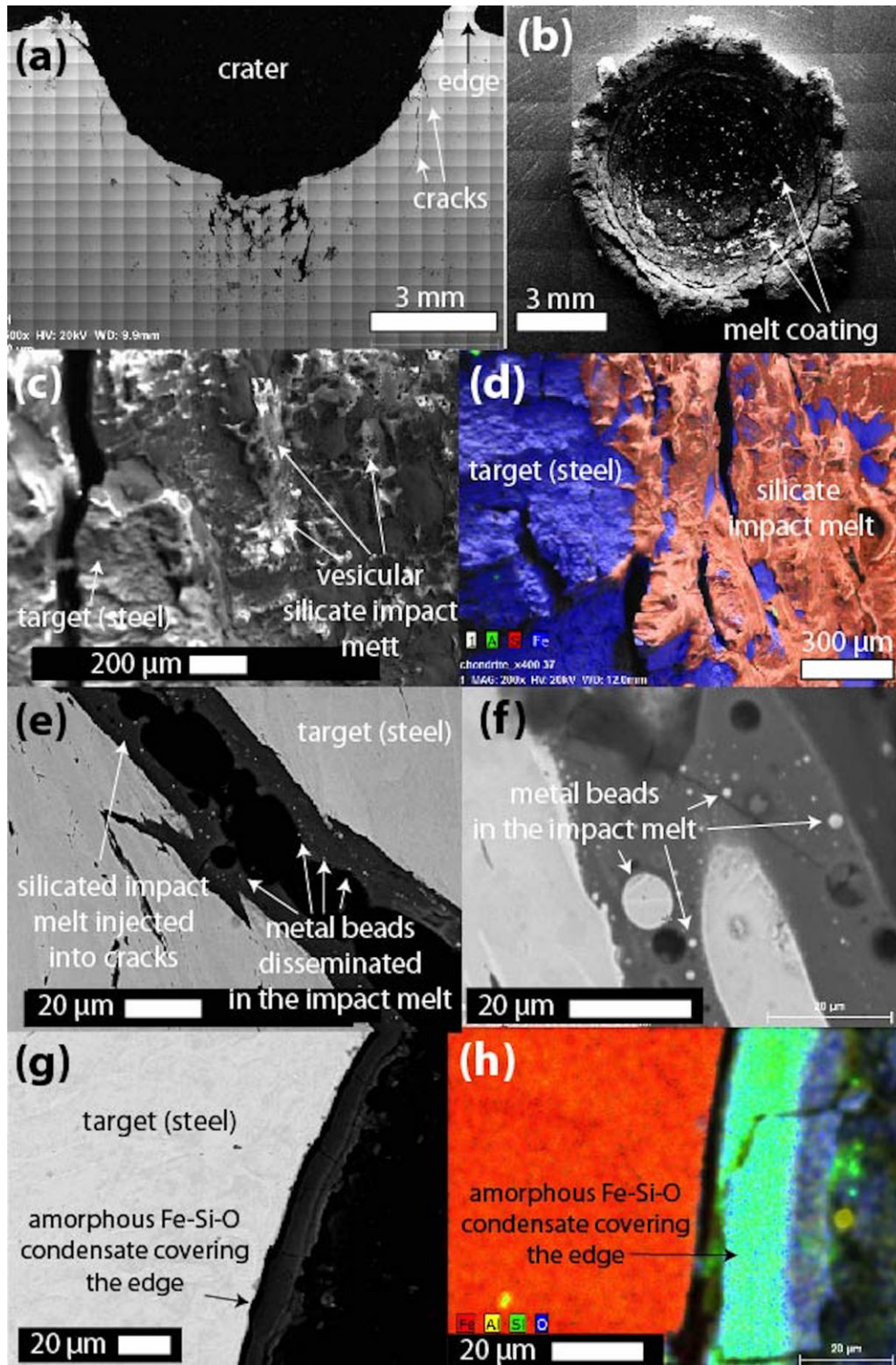


Fig. 2. SEM images of the targets after impact. a) BSE image of an orthogonal section of the major crater of experiment n0. b) SE vertical view of the major crater on the target of experiment n4. c) BSE image of impact melt covering the crater bottom. d) EDX-chemical map of impact melt covering the crater bottom. e) BSE image of fractures filled with impact melt containing beads of metal. f) BSE image of a detail of the metal beads contained in the impact melt covering the bottom of the crater. g) BSE image of the edge of the crater covered by a 10 μm thick condensate deposit (fayalite-ferrosilite composition). h) BSE image of an amorphous or poorly crystallized condensate covering the impact melt at the crater wall. (Color figure can be viewed at wileyonlinelibrary.com.)

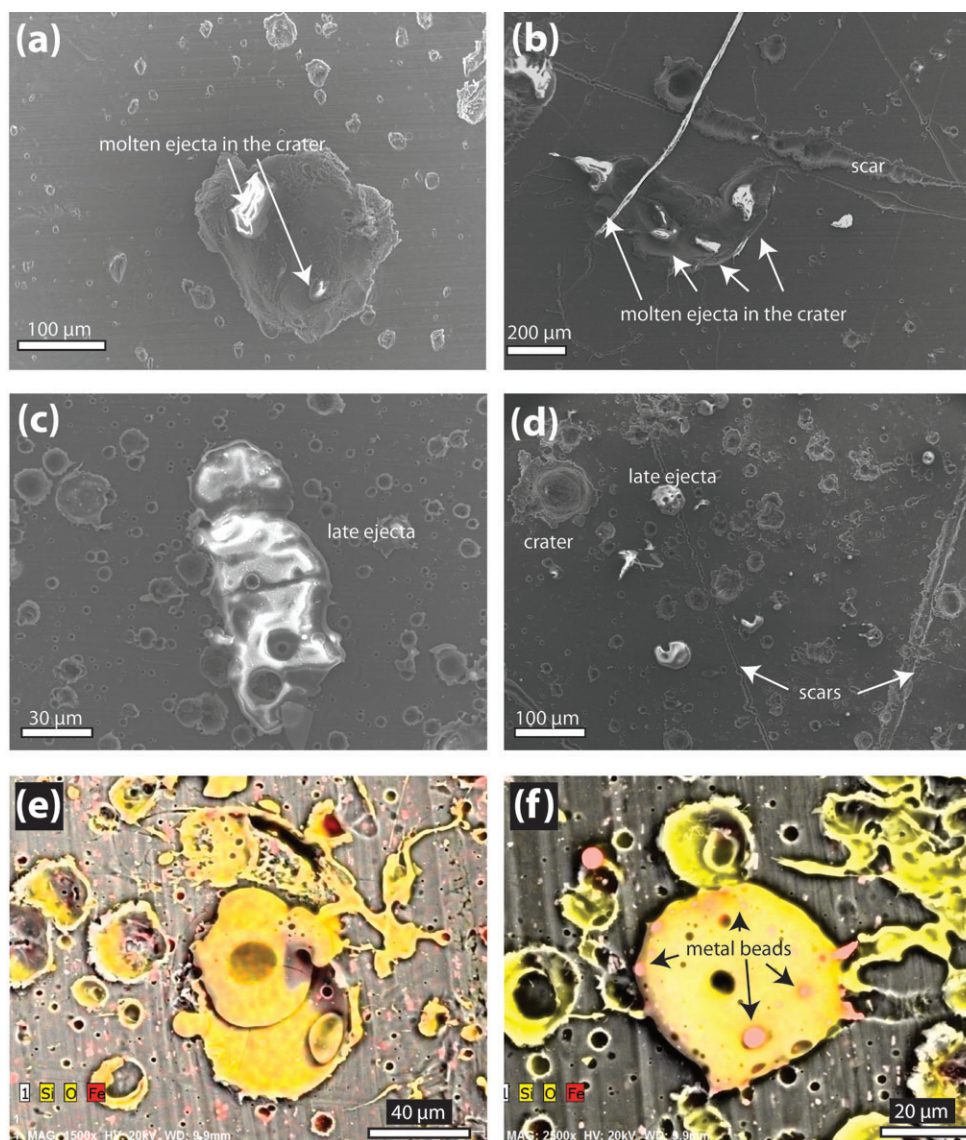


Fig. 3. BSE-SEM images of the aluminum ejecta catcher. a) Crater containing ejecta (quenched droplets of impact melt). b–d) Complex sequences of secondary craters and ejecta coatings. e, f) EDX-SEM chemical map (red = Fe; yellow = Si+O) combined with EDS image of the ejecta catcher showing the diversity of ejecta, their cumulation, and their textures including metal beads (f). (Color figure can be viewed at wileyonlinelibrary.com.)

ESEM with a LaB6 cathode and a BRUKER Quantax 655 detector, operated at 20 kV and 200 nA beam current at CEMEF-Mines ParisTech in Sophia Antipolis (France). EDX was used for semiquantitative point analyses. We assume an analytical precision of 1 wt% (Table 4).

Excitation volume is uncertain but close to $1 \mu\text{m}^3$. Therefore, the ejecta analysis does not cover the bulk of the ejecta but rather corresponds to a “point” ($1 \mu\text{m}^3$) analysis. If the ejecta were homogenous, it would provide information on the bulk of the ejecta. In the case of heterogeneous ejecta, which is generally observed (Figs. 3e and 3f), these analyses have to be

interpreted as mixing between the different endmembers. In the case of very flat ejecta samples (thickness $< 1 \mu\text{m}$), it is likely that there is a contribution from the aluminum ejecta catcher. For this reason, any conclusion on the behavior of aluminum is speculative with this experimental setup and has to consider the possible contribution of the witness plates.

Laser Ablation–Inductively Coupled Plasma–Mass Spectrometry

We analyzed trace element compositions in 112 ejecta by means of laser ablation ICP-MS. Due to analytical

Table 4. EDX-SEM major element compositions (wt%) of the ejecta, impact melt, and condensate layer.

	SiO ₂	Al ₂ O ₃	FeO	MgO	CaO	Na ₂ O	K ₂ O	TiO ₂
ejecta n3-001	48.3	16.5	5.17	5.10	5.12	8.51	10.5	0.75
ejecta n3-002	48.3	16.7	3.63	5.35	5.16	8.87	11.0	0.95
ejecta n3-003	50.1	17.0	4.10	4.84	5.46	5.83	11.6	1.12
ejecta n3-004	49.5	17.5	2.91	6.01	4.66	9.38	9.34	0.79
ejecta n3-005	50.7	18.3	2.85	4.31	6.47	4.16	12.0	1.24
ejecta n3-006	51.8	19.9	1.12	5.94	3.82	8.70	8.21	0.56
ejecta n3-007	48.6	21.8	2.53	5.29	4.81	6.44	9.77	0.69
ejecta n3-008	46.8	22.2	3.62	4.01	6.88	3.70	11.6	1.18
ejecta n3-009	47.5	22.9	2.28	4.26	6.38	4.52	11.1	1.13
ejecta n3-010	51.3	25.0	0.15	4.80	2.73	6.47	8.61	0.93
ejecta n3-011	53.4	25.5	0.13	3.88	1.70	6.55	8.41	0.46
ejecta n3-012	45.3	32.7	1.39	2.86	5.00	1.58	10.4	0.77
ejecta n3-013	34.7	32.2	6.55	7.69	4.82	2.47	10.9	0.65
ejecta n3-014	39.4	34.0	4.48	1.75	6.34	1.38	11.5	1.18
ejecta n3-015	22.7	31.2	10.6	2.29	10.0	4.21	16.9	2.07
ejecta n3-016	40.1	36.2	3.42	0.54	4.68	0.18	13.6	1.40
ejecta n3-017	41.8	38.8	1.31	4.44	3.15	5.22	4.65	0.61
ejecta n3-018	35.8	49.7	0.85	1.77	2.11	2.77	6.36	0.59
ejecta n3-019	31.1	54.6	0.66	2.59	1.65	3.52	5.30	0.59
ejecta n1-001	48.3	16.2	5.83	5.56	5.21	7.83	10.29	0.84
ejecta n1-002	52.5	17.2	1.85	5.72	4.94	7.09	9.75	0.95
ejecta n1-003	50.4	17.3	1.64	5.60	4.80	8.61	10.71	0.96
ejecta n1-004	50.4	17.5	2.98	6.31	3.91	9.93	8.19	0.80
ejecta n1-005	50.4	17.5	5.99	4.86	4.75	5.64	10.17	0.72
ejecta n1-006	50.8	18.4	2.54	5.94	4.42	8.23	9.19	0.52
ejecta n1-007	48.6	19.2	1.11	6.96	3.16	13.4	7.16	0.41
ejecta n1-008	48.7	19.3	2.10	5.64	4.24	9.35	9.96	0.76
ejecta n1-009	49.0	19.4	1.15	7.12	3.02	12.7	7.29	0.28
ejecta n1-010	48.4	19.4	2.71	5.64	4.81	8.50	9.71	0.81
ejecta n1-011	50.1	19.8	0.54	7.27	2.78	12.66	6.35	0.43
ejecta n1-012	51.0	20.2	1.67	6.23	3.93	8.29	8.16	0.58
ejecta n1-013	48.5	20.3	4.14	6.20	3.05	9.60	7.90	0.37
ejecta n1-014	50.5	21.8	0.40	7.59	2.45	11.3	5.93	0.13
ejecta n1-015	48.3	21.6	0.37	8.20	1.72	14.5	5.04	0.26
ejecta n1-016	51.0	22.5	0.44	8.00	2.38	10.2	5.34	0.21
ejecta n1-017	50.3	23.8	0.87	6.20	2.75	8.88	6.90	0.34
ejecta n1-018	49.8	24.0	1.07	5.79	3.46	7.49	7.94	0.40
ejecta n1-019	48.9	24.8	0.64	5.92	2.89	9.40	7.12	0.36
ejecta n1-020	51.6	26.1	1.05	4.65	4.02	4.04	7.92	0.55
ejecta n1-021	48.7	27.9	1.93	5.02	3.39	5.68	6.81	0.61
ejecta n1-022	48.5	29.4	0.74	3.71	4.05	2.99	10.1	0.55
ejecta n1-023	43.1	31.1	1.81	5.87	2.84	8.76	6.24	0.24
ejecta n4-001	54.4	22.5	2.87	5.91	4.15	4.57	5.01	0.52
ejecta n4-002	55.7	19.8	3.13	6.48	4.11	4.89	5.18	0.73
ejecta n4-003	54.0	20.0	3.31	7.30	3.94	6.20	4.79	0.42
ejecta n4-004	55.6	23.8	3.72	4.33	4.14	2.73	5.02	0.67
ejecta n4-005	50.0	16.9	3.98	5.76	4.45	8.56	9.72	0.70
ejecta n4-006	53.6	20.5	4.60	7.12	4.46	4.43	4.79	0.55
ejecta n4-007	54.8	19.5	4.70	5.12	5.24	3.07	6.49	1.04
ejecta n4-008	54.7	18.6	5.53	6.12	4.47	4.32	5.57	0.70
ejecta n4-009	53.0	18.9	6.04	6.44	5.05	4.18	5.63	0.73
ejecta n4-010	52.6	19.0	6.42	5.86	4.94	4.02	6.23	0.88
ejecta n4-011	50.9	20.6	7.83	4.69	6.23	1.91	6.64	1.22
ejecta n4-012	45.1	19.5	8.13	4.67	5.74	6.05	9.96	0.82

Table 4. *Continued.* EDX-SEM major element compositions (wt%) of the ejecta, impact melt, and condensate layer.

	SiO ₂	Al ₂ O ₃	FeO	MgO	CaO	Na ₂ O	K ₂ O	TiO ₂
ejecta n4-013	49.2	16.8	8.22	5.02	4.78	5.91	9.28	0.79
ejecta n4-014	48.9	14.8	10.1	4.70	4.68	6.17	9.85	0.76
ejecta n4-015	47.3	16.5	10.4	5.68	4.50	7.12	7.81	0.64
ejecta n4-016	43.6	27.2	12.7	5.34	4.10	2.70	3.64	0.65
ejecta n4-017	48.1	20.5	13.6	7.04	4.08	3.80	2.45	0.39
ejecta n4-018	49.1	18.3	14.8	5.92	4.52	3.10	3.67	0.70
ejecta n4-019	45.9	21.0	16.6	6.14	4.02	2.97	2.86	0.53
ejecta n4-020	42.3	26.5	16.7	3.19	5.31	0.69	4.47	0.91
ejecta n4-021	42.1	14.1	21.1	4.91	3.79	6.52	6.94	0.49
ejecta n4-022	34.6	20.8	32.9	5.05	2.87	1.78	1.54	0.48
ejecta n0-001	62.0	18.7	2.21	4.33	4.55	2.1	6.1	n.m.
ejecta n0-002	55.7	16.5	7.28	4.48	5.33	3.01	7.73	n.m.
ejecta n0-003	56.1	16.2	7.98	4.37	5.41	2.16	7.82	n.m.
ejecta n0-004	55.9	16.4	7.58	4.25	6.03	2.39	7.48	n.m.
ejecta n0-005	52.9	16.0	11.4	4.47	4.92	3.19	7.08	n.m.
ejecta n0-006	60.5	15.9	3.18	2.78	5.55	2.89	8.71	0.55
ejecta n0-007	61.8	18.2	2.15	3.56	4.31	2.37	7.01	0.55
ejecta n0-008	59.1	15.8	7.24	2.73	4.8	2.62	7.09	0.57
ejecta n0-009	54.0	15.6	14.1	2.45	5.26	1.80	5.94	0.84
ejecta n0-010	53.3	15.9	5.99	5.11	5.26	5.71	7.40	1.33
ejecta n0-011	42.5	11.3	24.8	4.07	4.36	6.23	5.95	0.80
ejecta n0-012	48.5	14.7	13.2	5.09	4.53	6.92	6.04	0.98
ejecta n0-013	48.1	14.1	12.2	4.91	5.02	6.91	7.71	1.09
ejecta n0-014	49.2	14.7	10.2	4.87	5.14	6.77	8.04	1.15
ejecta n0-015	43.5	12.7	19.9	5.31	4.40	8.32	5.11	0.76
ejecta n0-016	51.0	15.7	6.59	5.34	5.37	7.18	7.61	1.21
ejecta n0-017	51.3	15.7	6.36	5.28	5.33	6.99	7.83	1.20
impact melt crater 01	30.8	4.9	51.9	1.08	5.02	1.56	4.78	n.m.
impact melt crater 02	44.9	13.0	21.1	4.41	4.14	5.75	6.67	n.m.
impact melt crater 03	46.4	13.2	18.9	4.43	4.48	5.55	7.09	n.m.
impact melt crater 04	44.0	12.4	23.4	4.16	4.44	4.76	6.84	n.m.
impact melt crater 05	46.4	13.4	18.3	4.63	4.40	6.02	6.89	n.m.
impact melt crater 06	47.7	11.9	21.0	3.86	4.37	4.89	6.20	n.m.
condensate n0-01	23.8	n.m.	73.4	n.m.	2.83	n.m.	n.m.	n.m.
condensate-n0-02	39.6	n.m.	58.6	n.m.	1.81	n.m.	n.m.	n.m.
condensate n0-02	25.4	n.m.	73.3	n.m.	1.34	n.m.	n.m.	n.m.
condensate-n0-03	26.1	n.m.	72.3	n.m.	1.62	n.m.	n.m.	n.m.
condensate n0-03	22.6	n.m.	74.8	n.m.	2.62	n.m.	n.m.	n.m.
condensate-n0-04	24.0	n.m.	72.8	n.m.	3.25	n.m.	n.m.	n.m.
condensate n0-04	29.7	n.m.	68.5	n.m.	1.83	n.m.	n.m.	n.m.
condensate-n0-05	31.6	n.m.	66.7	n.m.	1.66	n.m.	n.m.	n.m.

n.m. = not measured.

constraints associated with the laser ablation setup, the smallest ejecta (with a surface $<10 \mu\text{m} \times 10 \mu\text{m}$) were not analyzed, but we selected samples covering a large size distribution (from about $100 \mu\text{m}^2$ to more than $50,000 \mu\text{m}^2$).

Trace element compositions of ejecta were measured at LMV Clermont-Ferrand using a ICP-MS Thermo Element XR equipped with a laser Excimer 193 nm Resonetics M-50^E with adjustable impact diameter (3–133 μm). Depending on the size of the analyzed ejecta,

the laser totally ablated it and the analyses can be considered as a bulk composition. This is not the case for all ejecta and especially for the biggest for which the analyses still have to be considered as “point” analyses that are representative of the bulk only if the ejecta is homogeneous, which is not the case (e.g., Figs. 3e and 3f). Four internal standards were used (610, 612, BR, VS-N), and the data were normalized to the mean Ca content measured with EDX-SEM in the population of ejecta. Laser ablation ICP-MS composition were also

Table 5. LA-ICP-MS trace element composition (ppm) of the ejecta and projectile.

	Ba	Ce	Co	Cs	Fe	Ga	La	Mn	Nb	Rb	Sc	Sr	Ta	V	Y	Yb	Zr
n3 ejecta 01	528	478	414	439	17926	174	442	332	402	505	179	443	442	395	439	485	411
n3 ejecta 02	498	456	396	412	18421	188	438	560	374	444	194	425	474	368	437	486	394
n3 ejecta 03	542	499	291	321	20523	159	463	782	398	367	187	466	511	373	484	527	436
n3 ejecta 04	522	500	155	398	16580	190	446	376	375	425	192	460	475	380	452	527	384
n3 ejecta 05	539	453	376	471	18699	164	449	492	417	517	177	451	488	375	467	493	435
n3 ejecta 06	529	460	382	450	18354	183	442	426	406	484	177	461	470	380	465	486	416
n3 ejecta 07	530	479	372	467	17742	183	455	412	412	507	182	456	479	390	468	493	418
n3 ejecta 08	529	476	371	397	18279	201	448	319	382	454	172	438	435	376	445	486	406
n3 ejecta 09	536	471	400	435	18669	188	456	336	410	503	177	457	464	381	462	504	429
n3 ejecta 10	556	486	398	434	19489	208	470	332	416	509	187	459	477	392	473	524	442
n3 ejecta 11	543	498	344	425	22669	193	454	363	404	471	177	456	468	381	452	488	410
n3 ejecta 12	552	510	367	447	17878	175	476	325	415	499	183	450	486	395	471	524	438
n3 ejecta 13	542	496	368	438	18686	204	469	429	420	476	178	474	478	379	481	496	422
n3 ejecta 14	535	476	337	458	20430	215	447	391	396	487	168	449	458	376	443	477	400
n3 ejecta 15	548	532	352	441	16306	151	448	379	395	468	176	454	485	387	464	493	424
n3 ejecta 16	530	461	371	428	16761	183	448	375	398	473	182	443	453	362	456	488	410
n3 ejecta 17	536	503	471	426	17311	171	462	335	403	486	181	456	459	386	467	505	425
n3 ejecta 18	539	495	399	418	17462	189	457	330	396	481	176	446	457	385	464	512	421
n3 ejecta 19	515	440	360	388	18208	198	420	304	367	460	170	431	414	375	443	481	402
n3 ejecta 20	552	486	422	460	17484	171	450	396	420	511	179	448	480	380	462	487	418
n3 ejecta 21	544	448	419	435	19630	245	432	515	374	490	165	460	456	405	437	487	397
n3 ejecta 22	555	570	116	517	14876	141	501	358	445	567	196	466	555	414	493	533	468
n3 ejecta 23	545	515	312	448	16197	168	469	379	410	479	181	459	486	388	475	512	423
n3 ejecta 24	567	533	278	489	15891	132	504	357	437	533	196	459	542	404	501	550	467
n3 ejecta 25	565	517	274	539	16052	153	488	389	427	591	187	460	532	397	481	524	454
n3 ejecta 26	532	518	372	422	16574	180	453	352	393	479	174	452	460	365	452	499	407
n3 ejecta 27	538	496	425	424	16049	166	463	322	394	483	179	444	448	375	464	507	425
n3 ejecta 28	550	501	305	433	15926	168	461	317	399	504	182	445	451	390	457	507	417
n3 ejecta 29	556	526	283	465	19085	210	476	358	411	503	181	472	483	397	467	497	429
n3 ejecta 30	567	484	381	431	16807	176	453	425	398	466	178	455	476	374	466	489	415
n3 ejecta 31	555	535	387	459	17248	196	473	347	398	498	173	461	481	383	470	523	415
n3 ejecta 32	557	544	365	469	17288	203	470	546	410	504	171	454	504	379	462	508	415
n3 ejecta 33	539	486	225	400	16727	197	451	335	385	436	166	457	462	364	446	493	389
n3 ejecta 34	545	478	378	453	18740	197	450	339	400	512	189	449	472	386	445	490	406
n1 ejecta 01	495	467	237	385	41325	136	441	391	403	453	179	409	427	371	429	474	419
n1 ejecta 02	498	425	395	421	20074	208	485	335	373	483	173	437	415	363	432	456	402
n1 ejecta 03	507	427	377	435	19934	186	427	362	380	488	176	437	436	358	435	463	402
n1 ejecta 04	490	432	281	383	17691	132	412	336	386	441	170	422	415	357	422	437	390
n1 ejecta 05	525	440	345	397	19925	164	433	350	379	458	178	449	428	368	437	494	393
n1 ejecta 06	519	407	364	383	19489	168	405	323	385	475	171	445	419	367	412	455	383
n1 ejecta 07	489	411	351	372	18769	181	405	314	366	461	170	434	388	366	411	436	379
n1 ejecta 08	514	428	330	364	17403	153	437	336	357	408	174	437	448	344	456	500	413
n1 ejecta 09	515	449	370	402	19140	185	439	320	386	443	182	453	440	356	445	492	408
n1 ejecta 10	487	417	381	371	17753	179	429	345	366	416	169	427	405	352	415	435	376
n1 ejecta 11	502	423	362	402	19467	171	442	346	381	438	171	439	425	356	428	460	401
n1 ejecta 12	567	475	290	447	20113	169	461	721	376	485	193	488	437	342	484	512	380
n1 ejecta 13	513	413	337	388	18716	151	456	435	374	430	169	460	441	338	439	464	398
n1 ejecta 14	493	402	314	392	16874	131	394	425	371	409	162	438	421	328	387	423	362
n1 ejecta 15	523	433	319	398	17331	150	437	380	375	429	177	455	435	341	446	470	386
n1 ejecta 16	516	419	274	393	17920	140	410	336	368	455	166	428	421	344	400	436	385
n1 ejecta 17	555	466	274	313	41328	134	459	645	363	342	182	454	445	312	474	511	400
n1 ejecta 18	479	363	295	258	55074	152	356	616	340	420	170	409	387	338	421	418	377
n1 ejecta 19	518	443	333	356	19777	150	446	389	377	406	181	460	453	359	451	487	412
n1 ejecta 20	542	458	338	386	19488	164	490	346	383	437	177	446	439	362	447	493	409

Table 5. *Continued.* LA-ICP-MS trace element composition (ppm) of the ejecta and projectile.

	Ba	Ce	Co	Cs	Fe	Ga	La	Mn	Nb	Rb	Sc	Sr	Ta	V	Y	Yb	Zr
n1 ejecta 21	537	471	367	434	21096	187	467	347	406	492	186	453	470	377	462	512	430
n1 ejecta 22	519	445	378	394	19321	182	450	373	395	442	187	461	468	362	454	499	424
n1 ejecta 23	517	424	367	334	20448	173	436	463	380	373	174	439	463	317	458	515	397
n1 ejecta 24	568	487	308	351	19456	138	528	827	374	395	194	483	538	340	502	565	429
n1 ejecta 25	542	456	345	393	23291	144	458	499	384	431	174	461	474	374	442	513	398
n1 ejecta 26	571	463	356	506	21606	179	456	632	417	554	170	464	471	380	423	475	376
n1 ejecta 27	494	401	347	419	16142	171	415	585	361	466	160	432	429	337	404	452	364
n1 ejecta 28	445	383	313	545	37853	242	378	953	321	608	167	397	368	352	390	407	337
n1 ejecta 29	535	455	377	424	18114	183	464	368	390	460	180	456	476	363	455	503	415
n1 ejecta 30	593	454	248	583	13910	149	409	596	324	591	146	436	356	309	365	423	270
n1 ejecta 31	582	374	225	1828	18892	339	395	1166	303	2067	154	402	398	410	356	422	339
n1 ejecta 32	552	446	234	375	15229	137	447	566	356	390	172	445	420	335	435	481	357
n1 ejecta 33	562	528	288	395	17985	150	481	381	396	461	186	460	468	387	454	518	417
n1 ejecta 34	577	491	377	437	17892	181	488	1406	415	466	187	484	495	364	468	532	409
n4 ejecta 01	542	503	368	397	20714	164	470	439	396	417	179	461	496	366	482	507	425
n4 ejecta 02	537	514	383	442	22854	186	452	420	395	470	171	459	468	368	449	491	409
n4 ejecta 03	488	379	166	396	13365	113	361	816	157	414	142	412	199	164	394	403	212
n4 ejecta 04	500	471	296	608	230913	267	430	2020	363	626	161	428	493	335	455	491	414
n4 ejecta 05	763	660	440	477	26828	227	651	931	507	512	231	638	660	434	684	726	556
n4 ejecta 06	616	535	366	407	26066	187	510	666	438	406	189	494	537	371	490	576	449
n4 ejecta 07	580	460	379	461	34999	197	433	624	407	477	171	444	483	363	423	495	385
n4 ejecta 08	545	501	299	428	89373	150	462	710	423	485	181	448	475	386	465	497	431
n4 ejecta 09	518	471	384	469	24606	201	422	410	364	518	163	443	419	349	427	445	366
n4 ejecta 10	479	416	326	484	35220	171	372	588	311	484	146	374	383	362	399	402	336
n4 ejecta 11	534	472	386	436	17602	176	432	355	373	496	168	432	448	355	434	488	413
n4 ejecta 12	520	486	294	354	332583	153	449	1852	360	373	175	395	437	377	420	481	382
n4 ejecta 13	559	445	383	471	23597	212	460	495	391	501	176	445	457	399	442	465	398
n4 ejecta 14	539	454	362	407	22350	183	442	501	373	434	173	440	430	367	436	478	380
n4 ejecta 15	545	460	363	436	25194	216	433	681	343	478	170	454	392	340	414	462	358
n4 ejecta 16	501	447	334	268	64679	146	423	565	370	304	171	436	449	319	477	468	398
n4 ejecta 17	580	529	367	393	57040	196	483	502	425	435	182	510	508	337	499	564	460
n4 ejecta 18	544	470	364	457	42276	181	451	632	370	471	176	419	466	364	435	495	399
n4 ejecta 19	552	467	396	438	19224	170	456	378	395	469	178	449	455	374	442	503	415
n4 ejecta 20	546	438	358	380	35420	166	431	599	339	374	165	424	436	350	403	481	345
n4 ejecta 21	547	422	262	431	47152	168	405	1081	261	434	150	453	308	243	419	466	288
n4 ejecta 22	506	427	399	446	33217	206	440	526	360	499	170	427	423	362	418	454	369
n4 ejecta 23	481	326	236	527	15958	183	328	1157	198	560	123	383	239	220	331	387	210
n4 ejecta 24	111	116	102	94	98	111	119	112	107	109	113	131	115	112	112	113	112
n0 ejecta 01	569	483	484	423	88764	249	473	709	424	546	180	503	497	365	501	503	441
n0 ejecta 02	592	491	537	869	76151	380	433	891	413	950	166	455	548	638	418	464	422
n0 ejecta 03	524	490	439	305	19669	201	449	343	383	357	177	450	453	294	450	486	412
n0 ejecta 04	536	491	432	327	19818	196	457	334	383	378	178	452	451	303	453	490	422
n0 ejecta 05	530	462	443	260	20439	215	445	386	393	307	181	452	450	259	451	481	420
n0 ejecta 06	516	462	423	368	22991	189	438	352	387	443	174	436	449	347	444	494	410
n0 ejecta 07	520	436	405	363	20590	185	440	367	371	415	176	436	421	340	452	462	388
n0 ejecta 08	539	493	423	422	24611	214	455	402	409	507	190	471	467	364	471	502	435
n0 ejecta 09	525	465	422	325	22626	192	451	332	383	371	183	449	451	318	453	501	425
n0 ejecta 10	545	450	407	304	21456	174	431	327	384	371	179	443	435	297	443	482	420
n0 ejecta 11	533	466	365	247	36669	153	457	435	385	276	176	433	470	258	450	494	403
n0 ejecta 12	535	477	391	315	40235	172	456	387	388	354	181	447	462	321	456	511	423
n0 ejecta 13	534	461	393	281	32408	176	445	369	373	321	180	443	442	288	451	493	415
n0 ejecta 14	531	447	323	232	37510	131	458	377	369	262	187	446	446	226	439	494	412
n0 ejecta 15	518	435	393	365	25335	184	427	335	374	417	173	435	418	345	427	460	394
n0 ejecta 16	530	465	433	379	49360	206	453	384	400	470	182	471	481	355	454	493	429

Table 5. *Continued.* LA-ICP-MS trace element composition (ppm) of the ejecta and projectile.

	Ba	Ce	Co	Cs	Fe	Ga	La	Mn	Nb	Rb	Sc	Sr	Ta	V	Y	Yb	Zr
n0 ejecta 17	532	462	416	375	18660	194	461	332	393	462	178	472	456	338	450	504	423
n0 ejecta 18	502	452	413	365	21110	189	444	365	384	443	169	463	466	323	455	484	414
n0 ejecta 19	508	441	396	357	21311	214	428	428	375	448	167	450	479	318	432	482	392
n0 ejecta 20	543	466	377	291	29140	178	433	350	383	330	171	440	439	277	444	484	410
Projectile 1	510	447	431	383	30452	205	446	342	381	476	164	453	435	341	429	485	402
Projectile 2	538	434	449	390	32849	221	425	340	383	478	172	452	453	355	438	497	399
Projectile 3	533	461	463	394	39532	200	464	404	402	509	178	480	479	373	464	507	421
Projectile 4	501	449	410	381	39112	187	427	488	380	408	167	420	459	339	419	465	381
Projectile 5	518	454	419	422	37710	201	440	459	371	457	168	444	446	354	423	469	389
Projectile 6	536	481	419	432	24611	200	443	432	371	479	176	447	452	356	445	487	397
Projectile 7	508	427	407	445	25667	224	399	717	348	488	160	439	409	375	412	448	379
Projectile 8	546	475	431	307	29786	187	465	353	392	342	185	456	477	288	450	502	421
Projectile 9	535	474	439	324	30434	207	460	371	396	367	183	454	478	299	451	494	412
Projectile 10	522	464	429	236	36660	150	465	344	376	278	192	438	449	272	440	494	407
Projectile 11	526	449	354	209	36612	145	448	352	358	243	182	434	461	176	424	470	412
Projectile 12	518	434	415	383	27950	187	431	316	370	418	175	434	415	346	429	486	393
Projectile 13	549	460	411	258	50549	169	443	393	377	264	189	449	440	278	455	495	416
Projectile 14	532	432	391	290	27659	196	431	313	355	316	179	425	455	303	426	482	381
Projectile 15	504	426	376	289	34898	169	422	314	359	327	181	423	425	307	430	470	391
Projectile 16	579	449	468	307	54295	229	455	422	407	358	201	476	516	310	482	500	418
Projectile 17	541	454	418	331	32756	187	445	365	386	380	184	444	476	313	447	490	415
Projectile 18	525	448	405	263	25002	175	444	325	361	291	177	447	422	287	434	486	386
Projectile 19	522	454	429	370	23304	207	436	337	396	480	168	481	448	335	486	506	429
Projectile 20	515	431	322	234	56242	119	423	406	379	243	182	470	420	261	477	491	433

measured for 20 points on the surface of a projectile (Table 5).

In addition to the laser ablation analyses, we analyzed the bulk composition of four projectiles to investigate the heterogeneity associated with the formation of this glass (Table 1). Major element oxide concentrations were measured by the CRPG laboratory in Nancy (France), using a Jobin-Yvon JY 70 inductively coupled plasma atomic emission spectrometer. The analytical method is similar to the one described by Govindaraju and Mevelle (1987). Details about analytical procedures and uncertainties are available at <http://www.crpq.cnrs-nancy.fr/SARM/index.html>. Most trace elements data are represented normalized to the composition of the projectile (mean from four analyses).

RESULTS

Description of the Target

All experimental runs resulted in a typical bowl shape crater (Fig. 2a). The diameter of the crater are 6.2, 8.5, 8.0, and 9.8 mm for the experiments n3 (190 J), n1 (444 J), n4 (710 J), and n0 (1899 J), respectively, suggesting a weakly positive correlation between the impact speed or the kinetic energy. Crater bottoms are

partially or totally mantled by a mixture of silicate glass (melted projectile; Figs. 2c and 2d) that represent quenched impact melt and metallic materials in various proportions (e.g., Fig. 2f). We observed numerous concentric fractures at the bottom and on each side of the craters (Figs. 2a and 2d). These cracks are deep and injected by impact melt that was likely emplaced during excavation stage (Fig. 2e).

We prepared a target (n0) sample for observations in the median plan of the crater, orthogonal to the surface of the target in order to monitor modifications at the bottom of the crater as well as crack propagations (Fig. 2). Strikingly, the geometry of fractures is typical of that found in natural impact craters in rocks (e.g., Kumar and Kring 2008), despite the rheology of our target (steel) is that of a ductile material and largely differs from the rheology of classical (brittle) rocks. The silicate glass formed by the quench of the melted projectile that covers the impact crater and injects most fractures (Fig. 2e) contains numerous small iron-rich metal beads (Fig. 2f). This impact melt also contains many spherical vesicles (Fig. 2c) that were not present initially in the projectile. The external edge of the n0 crater is covered by a 10 μ m thick iron-silicate amorphous or poorly crystalline oxide layer (Figs. 2g and 2h). This layer has a fayalite to ferrosilite composition (Table 4) and its

location (at the edge below the metal flaps) as well as its layered and continuous aspect make us interpret it as resulting probably from the condensation of the vapor plume after the impact (see discussion). These condensates also coat some places within the crater (Fig. 2h) but they are relatively rare and absent going out of the crater away from the crater rim.

Description of the Ejecta

The Al witness plates designed to collect the ejecta contain abundant impact pits, relatively abundant craters and ejecta, as well as some scars (Fig. 3). Some of these scars are linear but others have very curved trajectories.

The proportion of silicate ejecta coming from the projectile and iron metal-rich ejecta coming from the target is highly variable depending where the ejecta catcher is located. A few large iron-rich ejecta particles are responsible for the largest craters on the ejecta catcher (Fig. 1c). Roughly, we observed a nearly circular (Fig. 1a) ejecta field resulting from a conical ejecta blast where silicate ejecta were mostly inside the cone and iron ones near the sides of the cone. We cannot observe significant differences in the witness plates of the four experiments. We acquired a large-scale mosaic of X-ray chemical maps acquired on the Al witness plate, sampling the inner part of the impact ejecta field from experiment n4 (Figs. S2–S4 in supporting information). On these maps, using ImageJ, we counted about 40% generally small (1–10 μm) iron-rich ejecta versus 60% generally larger (5–50 μm) silicate ejecta. Like for the impact melt observed on the target, the ejecta contain numerous small iron metal beads (Figs. 3e and 3f).

Structural Modification of the Target

During the formation of the crater, the steel target was deformed (e.g., folded crater rim). A significant mass was excavated and collected as ejecta and possibly as condensates. The surface of the target was injected and covered with the melted projectile, which changed drastically the bulk composition of the first micrometers of the target surface. Because of the coating, the surface is now composed of silicate impact melt instead of iron metal.

Major Element Composition of the Ejecta and of the Impact Melt Covering the Crater

Ejecta are very heterogeneous between silicate-rich projectile composition, iron target, and aluminum contamination from the ejecta catchers as three endmembers (Fig. 4).

Low-velocity shots (n3 and n1) produced mainly projectile-dominated ejecta, as they closely follow mixing trends between the projectile and Al witness plate. On the other hand, the high-velocity shots (n4 and especially n0) show mixing between projectile and target composition. Moreover, most are large droplets of solidified silicate liquid that contain various amounts of small iron metal beads (Figs. 3e and 3f). Point analyses (Table 4) have to be interpreted considering this heterogeneity: the point analyses are sampling an equivalent ionization region of about $1\ \mu\text{m}^3$, a volume that can include or exclude metal beads (some of which are not visible because they are below the surface) and a possibly significant contribution from the Al witness plate composition.

Aluminum has a high level of enrichment in some ejecta (up to 54.6 wt% versus ~ 13.4 wt% in the projectile), as expected when analyzing a thin sample with contribution from the aluminum ejecta catchers. This contribution may be related to the small thickness of the ejecta and is particularly important for the experiments with the lowest impact energies (Figs. 4a and 4b). In the high-velocity experiments (n4 and n0), some ejecta are strongly enriched in iron (up to 32.9 wt% FeO_{tot} in the ejecta versus 4.14 wt% $\text{Fe}_2\text{O}_{3\text{tot}}$ equivalent to ~ 3.73 wt% FeO_{tot} in the projectile). We note that some point analyses of ejecta show a very low Fe content, together with a limited contamination from the Al-catcher. Here mixing between the three endmembers (projectile–target–Al-catcher) cannot result in such composition.

The composition of the impact melt covering the crater in experiment n0 is comparable to the composition of the ejecta (Table 4).

Composition of other elements is generally close to the nominal composition of the projectile within a 5% error-bar. It evolves passively following the dilution/concentration associated to the enrichment/depletion in iron and contribution of aluminum from the ejecta catcher (Fig. 4).

Trace Element Analyses

Trace element analyses of four bulk projectiles show their composition is very homogeneous (Table 1; Fig. 5a) demonstrating that the process involved in the formation of our starting material resulted in glassy beads with identical trace element contents. Contrary to this, the 20 analyses of another bead using LA-ICPMS show a larger spread, especially for volatile elements. The trace element pattern normalized to the mean bulk of the projectile is relatively flat (Fig. 5b), but the absolute compositions are significantly lower than expected. The precise position of the pattern is

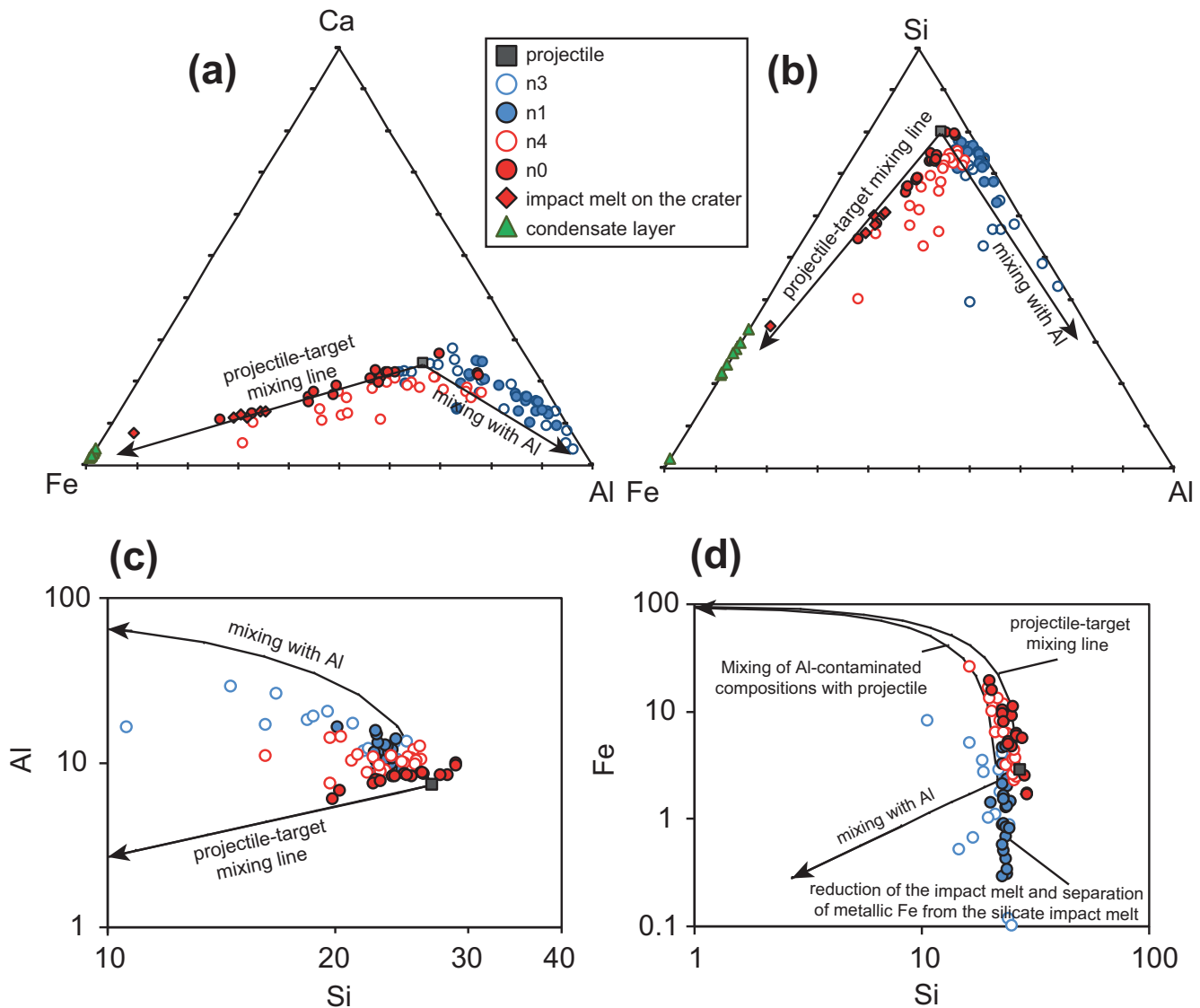


Fig. 4. Major element composition of the ejecta of the experiments n3, n1, n4, n0 (sorted with increasing energy of impact), and of the projectile. a) Triangular Ca-Fe-Al plot. b) Triangular Si-Fe-Al plot. c) Si versus Al plot. d) Si versus Fe plot. Data are in atom%. (Color figure can be viewed at wileyonlinelibrary.com.)

dependent on the normalization and as mentioned above, here we used the mean Ca content measured with EDX-SEM. This measurement is unfortunately poorly constrained because it is semiquantitative. For the discussion, we will avoid interpretation of absolute composition and will focus on the slope and spread of our analyses. Tracking subtle trends, the projectile analyses display a limited depletion in volatile element resulting in a global negative slope (Zr/Rb generally >1 ; see Figs. 6a and 6b). This slope is related to a depletion in the volatile element only (Ba to Rb; Fig. 6c) and the refractory element remains unfractionated (Fig. 6).

The chemical composition of the ejecta collected from the experiment n3 (lowest energy) normalized to

the measured composition of the projectile displays a nearly flat pattern (Fig. 5c) when elements are sorted by increasing volatility (Lodders 2003). The spread of the 34 analyses is slightly more important for volatile elements (Co, Ga, Rb, and Cs). The ejecta collected from the experiment n1 display a very similar pattern of trace element composition, an outlier having extreme enrichment in Ga, Rb, and Cs. The 33 other spectra are nearly perfectly flat. n4 also present a population of flat spectra, but the spread of composition is more pronounced here. An unique pattern is especially low and represents an outlying measured composition. Nevertheless, even for this pattern, there is no continuous slope expected for a volatility-controlled

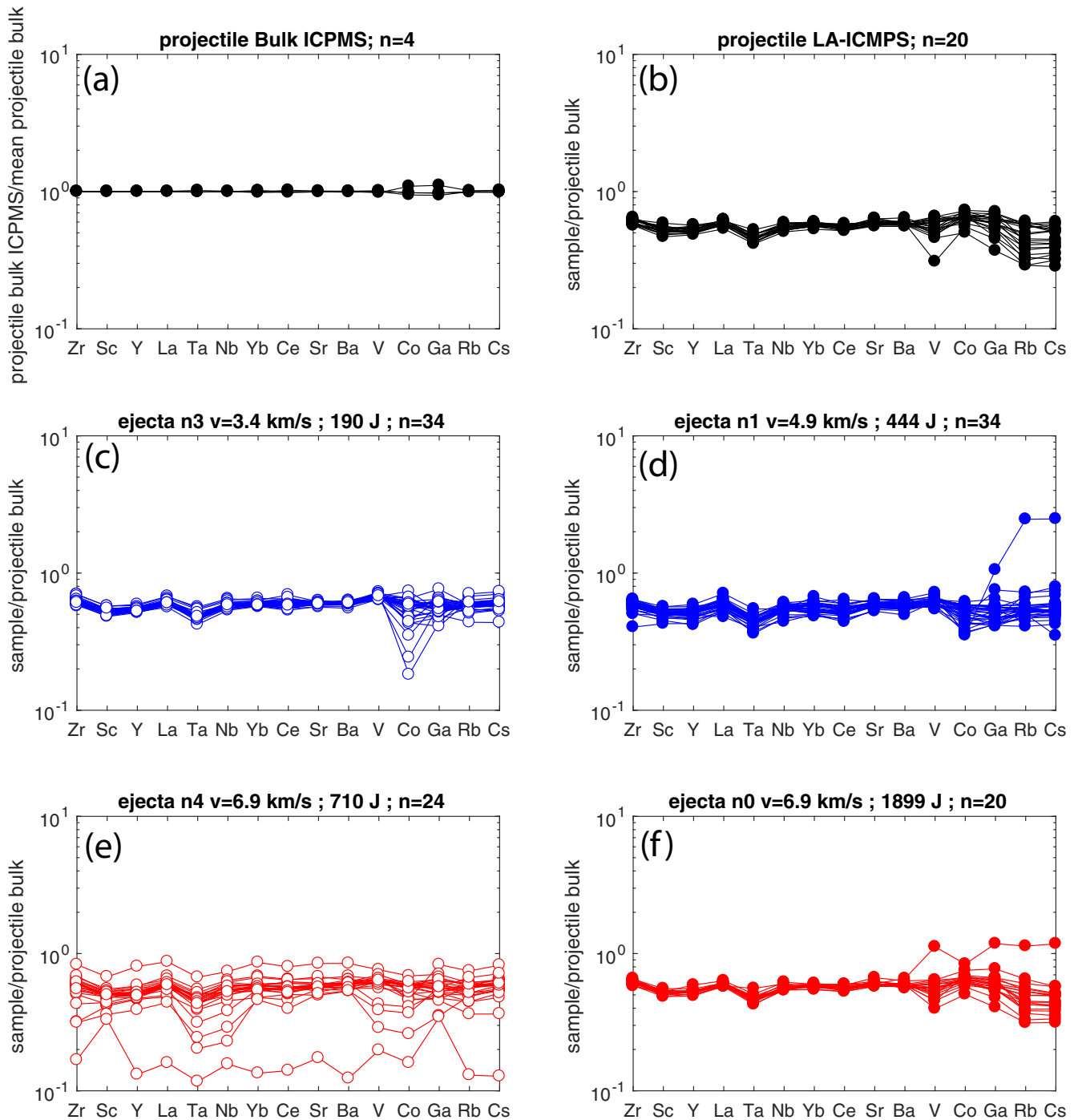


Fig. 5. Trace element composition of the projectile and ejecta. a) Bulk composition of four beads of phonolitic glass prepared as projectile determined by ICP-MS. b) LA-ICP-MS analyses of a projectile normalized to the mean bulk composition. c–f) LA-ICP-MS analyses of the ejecta collected on the ejecta catcher in experiment n3, n1, n4, and n0 normalized to the mean bulk composition of the projectiles. The elements are sorted according to volatility (Lodders 2003). (Color figure can be viewed at [wileyonlinelibrary.com](http://onlinelibrary.com).)

fractionation and it is nearly flat except unexplained interelement fractionation (e.g., when comparing Ga and Sc to Rb and Cs). The ejecta from the highest energy experiment (n0) display relatively flat pattern

too, with larger spread of the data as in all other cases. When looking into detail on the trace element pattern of all these patterns (Fig. 6), it appears that the ejecta share similarities with the projectile composition

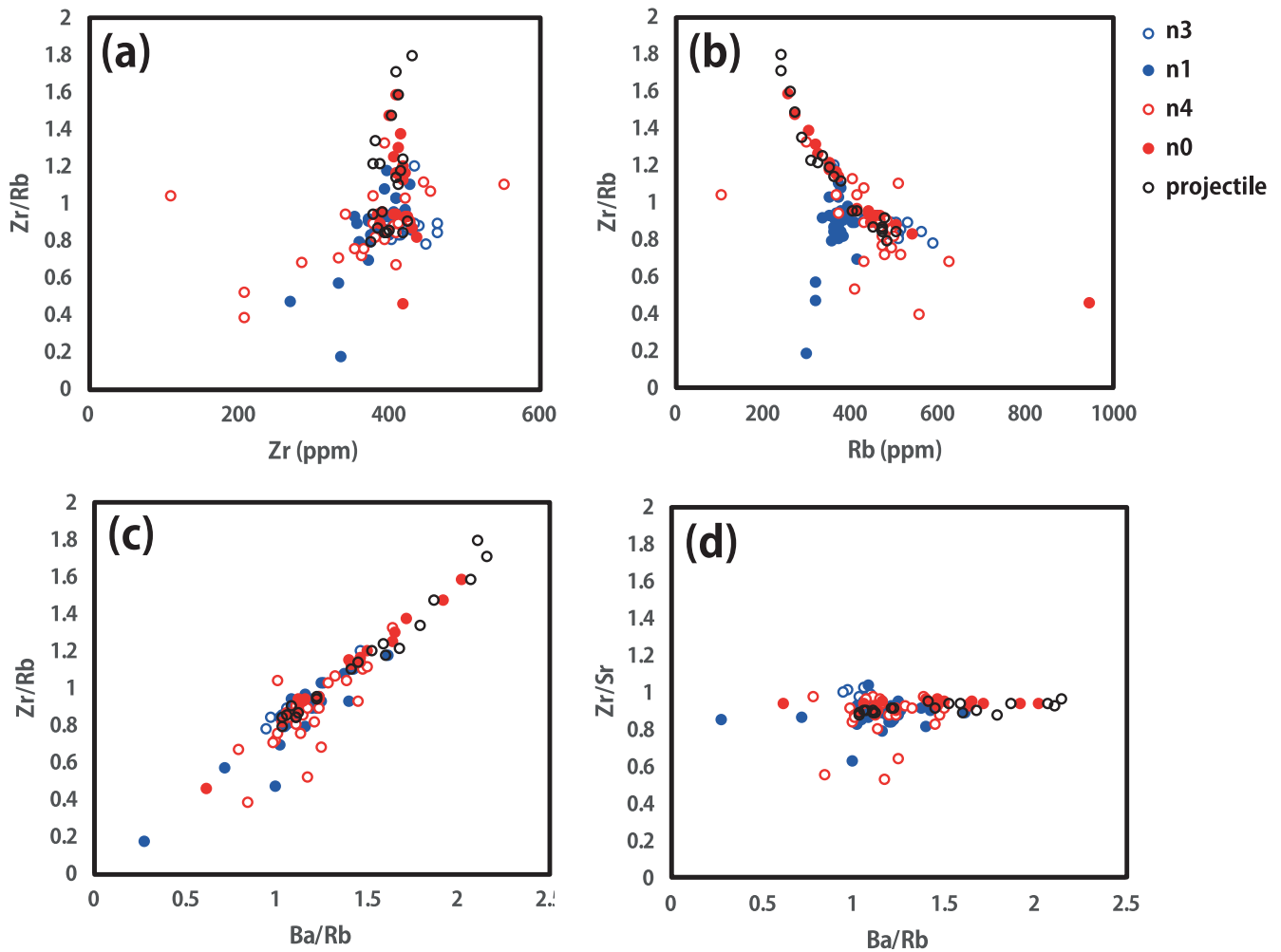


Fig. 6. (a) Zr/Rb versus Zr, (b) Zr/Rb versus Rb, (c) Zr/Rb versus Ba/Rb, and (d) Zr/Sr versus Ba/Rb diagrams comparing the composition of ejecta from experiment n3, n1, n4, n0 with the composition of the projectile. (Color figure can be viewed at [wileyonlinelibrary.com](http://onlinelibrary.wiley.com/doi/10.1111/maps.13131).)

analyzed with LA-ICP-MS (Fig. 5b): a generally slightly negative slope mainly supported by a depletion in volatile elements. As these specificities are not observed for bulk analyses (Fig. 5a), they are the result of an analytical technique bias.

To identify fractionation trends independent to the analytical technique, we normalized the mean composition of the ejecta to the mean composition of the projectile measured with LA-ICP-MS. We calculated the error propagation and plotted the 2σ error bars. The results show here that there is no chemical fractionation with volatility whatever the impact energy and speed of the projectile within the ranges of these experiments.

Finally, LA-ICP-MS analyses (Table 5) provide a duplicate of iron content for the population of ejecta that confirms the results from EDX analyses. Again, when compared to the measured composition of the projectile, most ejecta are moderately depleted in iron in all

experiments but a few are found to be highly enriched in experiments performed at the highest impact velocities.

DISCUSSION

Time Scale Associated with the Cratering Process

The shock process and the accompanying release to ambient pressure occur on a very short time scale, and there is not enough time for chemical diffusion to produce the observed textures and chemical variations. Under our conditions, pressures are expected between 50 and more than 100 GPa (see tables 4.1 and 4.2 in Melosh 1989) and the shock wave-compression maximum temperature can be roughly estimated at 2500 to more than 3000 K using iron metal Hugoniot curve (Ahrens et al. 1998). Assuming a ductile behavior for the steel target, it is remarkable that this set of

experiments produced impact craters in every aspect similar to natural impact craters on geological (fragile) rock targets showing characteristic cross sections (Fig. 2a) with an impact melt layer glazing a shocked/compressed and fractured basement (Melosh 1989; French 1998).

The systematic occurrence of vesicles and metal-bleb-bearing impact melts in craters, the collections of metallic- and phonolitic-dominated ejecta on the witness plates, as well as the existence of iron-silicate amorphous or poorly crystalline condensates on the external part of the flap of the crater confirm that melting, degassing, reduction, evaporation, and condensation are some of the physical/chemical processes involved in hypervelocity impacts. A rough estimate of the duration of contact and compression stage is approximately $2L/V$, where L is the dimension of the projectile and V is the impact velocity (Melosh 1989). The diameter of the projectile being 2.8, 2.97, 2.77, and 3.8 mm in our experiments, durations of 1.7, 1.2, 0.8, and 1.1 μ s for experiments n3, n1, n4, and n0, respectively, can be calculated. Adding a few other μ s for the completion of the excavation and the modification stages of impact crater formation gives the order of magnitude of the duration of the impact crater formation together with the time for launching the ejecta and collecting them on the Al witness plates. Such an exceptionally short-lived duration emphasizes the intricacy of the problem to be solved.

Impact Melt Properties

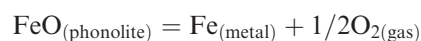
Crater Surface Coating

During the impact, a significant portion of the melted projectile largely sticks to and covers the inside walls of the impact crater, forming a thin layer of impact melt. A smaller amount is injected into the concentric cracks of the crater and the remaining is ejected as small droplets, some of which being quenched and collected on Al witness plates.

Owing to the cross section cut through the impact crater of the experiment n0 (Fig. 2a), estimates of the different materials produced by hypervelocity impacts are thus possible. For a very conservative averaged thickness of ~ 10 μ m layer of melted projectile covering the crater (Fig. 2f), one can calculate that the 5 mm diameter quasi-hemispheric crater is covered by ~ 3.1 mm³ of melted projectile. This volume represents close to 10% of that of the projectile (29.6 mm³). The remaining $\sim 90\%$ are either ejected out of the crater together with target material, or injected into the cracks in the metal target at the bottom of the crater, or evaporated/recondensed (Figs. 2g and 2h)—the latter portion being negligible in all cases.

Formation of Iron Metal Bead

The processes involved in the formation of the abundant small iron beads remain unequivocal. At least a part of them were separated from the melted target material and participated in an emulsion with the silicate liquid. Figure 2f clearly shows the incorporation of tiny iron metallic spherules into the impact melt. Examples are described in natural craters where iron metal sphere is also observed disseminated in silicate impact melt (e.g., Meteor Crater and Wabar, respectively, described by Mittlefehldt et al. [2005] and Hamann et al. [2013]). A second hypothesis is that some of these metal beads would result from the reduction of FeO from the phonolitic impact melt into Fe metal. With this process, we expect that after the separation of immiscible iron and silicate melts, the remaining silicate liquid would have lower iron content than the initial phonolitic composition. This assertion is supported by some local iron depletion in both the phonolitic impact melt and the ejecta. Figures 4a and 4b show that most compositions observed in the ejecta are the result of the mixing between three endmembers (projectile–target–aluminum from the ejecta catchers), but many of them display an iron-poor composition that cannot be explained by a simple contamination from the ejecta catcher. Here we propose that part of the iron beads formed by the immiscible separation of iron metal liquid after reduction of FeO from the starting phonolitic material. When analyzing the ejecta using EDX-SEM, in some cases, the “point” analyses sampled the residual silicate melt (without or with few metal beads) with extracted iron explaining low concentration. The ubiquitous occurrence of vesicles in the impact melt further hints that the reduction processes obey to a general reaction of the type:

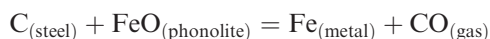


Even some vesicles might simply reflect boiling of the melt or volatilization of most volatile components in the starting phonolitic material. We propose then that the metal beads formed by the two abovementioned process. As the two origins are expected to form similar composition (nearly pure iron beads) and as the iron beads are very small and cannot be analyzed ruling out the possible contribution of surrounding silicate liquid, we failed to estimate the relative importance of reduction versus separation of melted target material.

Redox reactions are already documented during shock/impact experiments (Rowan and Ahrens 1994; Ebert et al. 2014) and natural impactites (Hamann et al. 2013) and are here confirmed as occurring within the impact time scale. Such process is observed in tektites and other types of impact glasses that are reduced

compared with the precursor target material (Lukanin and Kadik 2007). High temperatures (>2000 °C) reached at a certain stage of decompression are required for the occurrence of reduction reactions involving iron, the complete melting, and partial evaporation of the impact melt. In the present set of experiments, the reduction of shocked glass may be also attributed to the high temperature of the impact process. In the Ellingham diagram, the slope of the plots $d\Delta G/dT$ is positive for all metals, with ΔG always becoming more negative with lower temperature. Since these reactions are exothermic, they occur at lower temperatures. At high temperature, the sign of ΔG may invert and the oxide can spontaneously reduce to the metal. Then, for a given redox condition, the higher the temperature, the more reducing the conditions.

Other possible concomitant reducers include C and Si from the steel target. When reacting with the projectile, they produce transient reducing conditions in the impact melt in the vicinity of the C/CO at high temperature according to the following reactions:



In addition to the possible contribution of the melted target, shock-induced reduction of impact melt, i.e., here at the IW buffer curve or below, should thus be considered a viable mechanism for the formation of metallic phases.

Chemical Modification of the Impact Melt

The composition of the ejecta normalized to the composition of the projectile (Fig. 7) displays a flat spectrum. In the frame of uncertainty related to this kind of experiment and analytical procedure, we did not observe any chemical fractionation controlled by volatility in the ejecta, whatever the impact energy and speed of the projectile. Contrary to what is observed in Joule melting experiment where volatile elements are strongly fractionated (e.g., Floss et al. 1996), and contrary to what is described in experiments involving high-temperature pulse heating of silicate (Gerasimov et al. 2005) here no clear fractionation trend from volatility is observed (Fig. 7). It is very likely that the instantaneity of the impact limits the evaporation and avoids fractionation from volatility. The duration of the impact plus the relaxation time is very short (order of magnitude is $\sim 1 \mu\text{s}$; see calculation above), and not enough to promote significant vaporization through diffusion in the silicate liquid of the impact melt. These few 10^{-6} s are for instance three orders of magnitude lower than the few 10^{-3} s experienced in laser pulse experiments where some fractionation is described

(Gerasimov et al. 2005). With diffusivity in the order of $10^{-10} \text{ m}^2 \text{ s}^{-1}$ for most major elements in silicate melts (Eisenhüttenleute and Allibert 1995), the characteristic length for diffusivity ($l = \sqrt{Dt}$) is about 0.03 μm . The extremely low mobility of elements at such time scale provides, as a first approximation, a satisfactory explanation to the inefficient vaporization and the absence of significant volatility-controlled fractionation.

This result has however to be nuanced. As already mentioned, we observe in addition to the impact melt (n0 experiment), a thin layer of condensates (1–10 μm), especially at the edge of the crater (Fig. 2g) and also in other locations covering the impact melt (Fig. 2h). This feature unambiguously indicates the occurrence of a furtive vapor phase during this impact process. Instantaneous condensates being not representative of the bulk vapor, we have very little information about the vapor phase composition. Our analyses of the amorphous or poorly crystallized condensates indicate high Si, Fe, and O contents and a bulk composition varying from fayalite (Fe_2SiO_4) to ferrosilite ($\text{Fe}_2\text{Si}_2\text{O}_6$). Such compositions show that the vapor has been at least formed from the major elements at the point of impact, namely Si and O from the phonolitic projectile and Fe from the metallic target. This allows us to set corresponding partial pressures of this vapor phase, $\text{PSiO}_{(\text{g})}$, $\text{PFe}_{(\text{g})}$, and $\text{PO}_{2(\text{g})}$, the latter being supposedly closed to oxygen fugacity imposed by the IW buffer curve or slightly below (see 5.2). This vapor with a scarce and very thin thickness of the Si-Fe-O-rich amorphous or poorly crystallized condensates is, however, not supposed to weight too much in a mass balance calculation nor in any volatilization processes (Fig. 5). Our result suggests therefore that while a vapor phase was present at least during the n0 (the most energetic) impact experiment, its mass abundance per time unit must be negligible.

Mixed Ejecta Spray

The whole ejected material includes both the excavated ejecta from the steel target and the ejecta coming from the projectile. Precise quantification of the material excavated from the target from the collected ejecta on the witness plates is so far impossible, since a few large steel ejecta with grazing angles and constituting probably the main mass (see the first images with the very high-speed camera, Fig. 1) have not been collected. Nevertheless, from the diameters of the craters and assuming a hemispheric shape, we estimate that the excavated volume is about 124, 321, 268, and 493 mm^3 for experiments n3, n1, n4, and n0, respectively. With the hypothesis that 90% of the volume of the projectile was ejected, the population of ejecta consists of 4–9 vol% ejecta from the phonolitic projectile and 91–96 vol% ejecta from the target. As

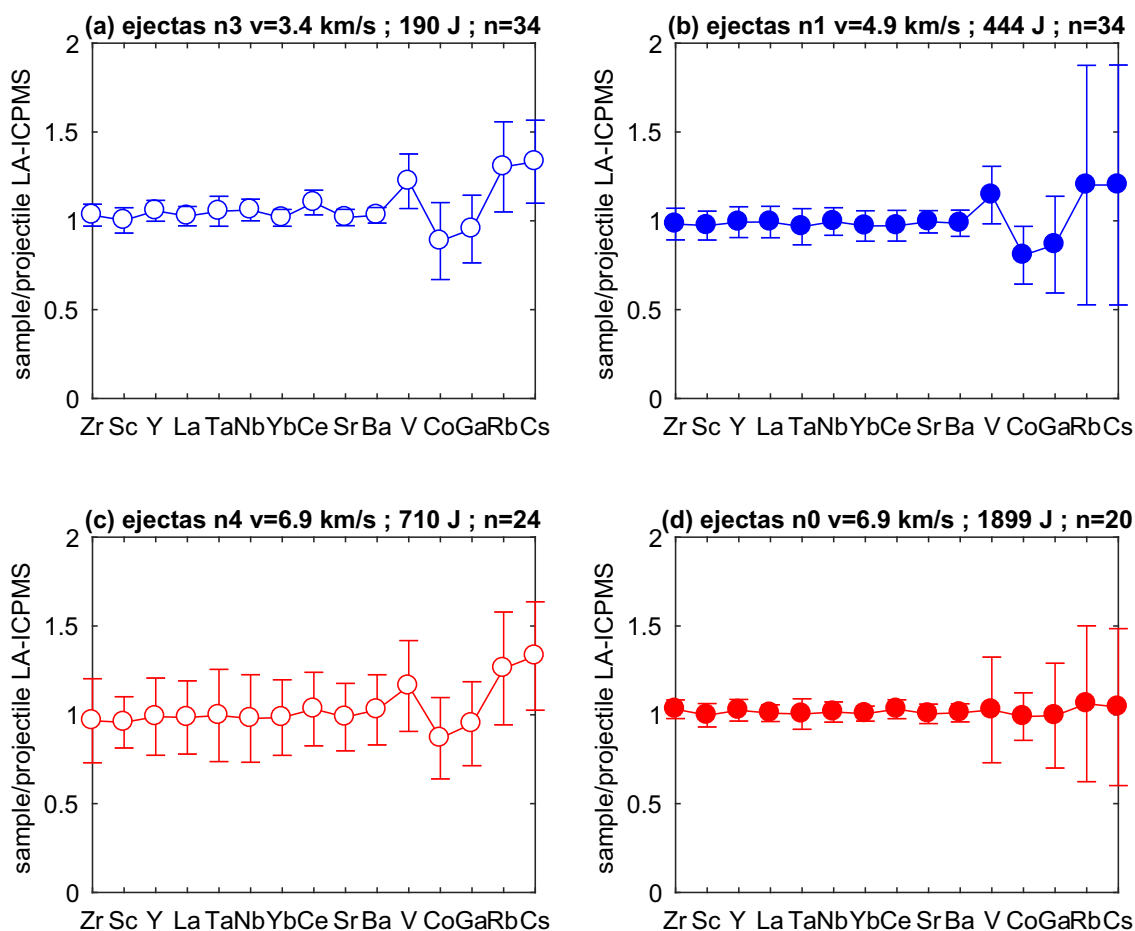


Fig. 7. Mean trace element composition of ejecta from experiment (a) n3, (b) n1, (c) n4, (d) n0 normalized to the mean composition of the projectile measured with LA-ICP-MS. Error bars are 1σ standard deviation. (Color figure can be viewed at wileyonlinelibrary.com.)

explained, the population of collected ejecta comprises both fragments of metal excavated from the target and silicate pieces of the projectile. The intense cratering of the target as well as the screening and scratching of our ejecta catcher show the complexity of the ejecta trajectories.

The ejecta catchers show both quenched droplets from silicate ejecta from the impact melt, and quenched iron droplets that were formed by the reduction of FeO in the projectile or directly separated from the target. Our current experimental setting prevents us from performing a global description of the distribution of silicate versus metallic ejecta, especially because we can observe only a small portion of the ejecta that is not necessarily representative of the entire blast. Nevertheless, during the blast, these two chemically and physically contrasted types of materials (silicate and metallic droplets) travel together from the target to the ejecta catchers as a dual spray. Mixing occurs between the two types of droplets, resulting in the formation of silicate ejecta including small iron spheres (Fig. 3f).

Mechanical Mixing of Target and Projectile Material as the Main Source of Chemical Change

As many ejecta contain beads of metal, our analyses show a large scatter for iron (and to a lesser extend manganese) contents. It is noteworthy that the mean composition of the silicate ejecta analyzed with EDX-SEM is sometimes depleted in iron, independently from a simple dilution that could be linked to aluminum contribution by the ejecta catchers. This depletion cannot be explained by uncertainty of EDX measurements (± 1 wt%). For instance, ejecta n3-010 and ejecta n3-011 have, respectively, 0.15 and $0.13 \pm$ wt% FeO (versus 4.06 wt% Fe_2O_3 equivalent to ~ 3.65 wt% FeO_{tot} in the projectile) and limited contribution of aluminum from the ejecta catcher (25.0 and 25.5 wt% Al_2O_3 versus 13.8 wt% Al_2O_3 in the projectile).

Nevertheless, we interpret the contrasted iron composition of ejecta as the result of a random sampling of iron-depleted silicate ejecta without metal bead (lowest iron contents) or metal bead-rich (highest

iron contents). The inhomogeneity produced by silicate–iron metal melt unmixing shares similarities with the silicate liquid immiscibility common in the evolution of natural impact melts (Hamann et al. 2017). In our experiments, the chemical heterogeneity is shared between EDX-SEM (“point”) analyses and ICP-MS (“bulk” in some case) analyses, illustrating that ejecta are heterogeneous (beads are not uniformly distributed in the ejecta) and of contrasted bulk compositions. This chemical heterogeneity is the result of the mechanical mixing of the melted projectile and the melted target ejecta (explaining high Fe contents) and of unmixing of iron liquid after reduction of FeO in the impact melt (explaining low Fe content in the residual impact melt).

We interpret these contrasted chemical compositions in a magmatic perspective. In the low-velocity experiments (n3 and n1), from the primitive composition of the projectile, the silicate liquid forming the ejecta sometimes lacks a significant portion of FeO that was reduced into the iron metal beads. Contrary to that, for the high-velocity experiments (n4 and n3), the silicate liquid was in some cases highly contaminated by iron metal from the target. Three distinct compositions can hence be produced, i.e., (1) the primitive composition of the projectile (FeO = ~4 wt%), (2) the composition of the silicate liquid depleted from iron after reduction and unmixing of iron melt, and (3) the composition of the silicate liquid doped in Fe from the target. If the redox conditions would allow oxidation of these iron metal beads into FeO and their incorporation into the silicate liquid, this third composition would be abnormally enriched in iron. We computed the temperature at liquidus and crystallization sequences for these compositions using MELTS (Ghiorso and Sack 1995; Asimow and Ghiorso 1998). From the primitive phonolitic composition ($T_{\text{liquidus}} = 1281$ °C, crystallization sequence computed with MELTS = spinel, leucite, olivine...), the composition of some ejecta evolved to iron-rich foidite ($T_{\text{liquidus}} = 1379$ °C, crystallization sequence = leucite, spinel, olivine...) and iron-poor phonolite ($T_{\text{liquidus}} = 1284$ °C, crystallization sequence = spinel, olivine, leucite). We show here that the major element heterogeneity results in a large temperature range for liquidus (1281 °C to 1379 °C) and different crystallization sequences. If not quenched, the droplets of silicated liquid that formed the ejecta would have developed very contrasted mineralogy. Depending on the cooling rate, largely related to its volume, the impact melt can crystallize and form a magmatic rock or be quenched as a glass.

To scale one, our experiments mimic impact cratering of (micro-) meteorites on metallic targets, and in this sense, may resemble processes at work on metallic (M-type) asteroids, like (16) Psyche. We can

expect that the surface of such bodies could be more or less coated by glassy or partially crystallized impact melts from the various impacting (micro-) meteorites, mostly chondritic. This feature could have important implications on the spectral signature of these objects, which may give information on the veneer rather than the main body composition.

However, more numerical and modeling works need to be done to extrapolate this kind of small (laboratory-scale) impacts to larger (beyond laboratory-scale) impact cratering, which would greatly contribute to our better understanding of the formation and evolution of metallic asteroid surfaces. Laser experiments could bridge part of this gap (Ebert et al. 2017). If our results can be extrapolated to larger object such as asteroids, they confirm (after Kelly et al. 1974; Gibbons et al. 1976; Horz et al. 1989; Mittlefehldt et al. 1992, 2005; Evans et al. 1992; Wozniakiewicz et al. 2011; Ebert et al. 2011, 2013, 2014; Hamann et al. 2013, 2016a, 2016b, 2017) that high-speed collisions between two distinct objects result in impact melt and ejecta, which compositions correspond to mixtures between the two colliding objects acting as geochemical endmembers, and having a large variety of liquidus temperature and crystallization sequences (i.e., contrasted mineralogy). The high-velocity experiments presented here provide evidence that the mechanical mixing of colliding objects depends on the impact energy.

Impact energy and especially impact velocity is primarily governing the amount of vaporization of the projectile and part of the target. In the case of the Moon, impact of micrometeorites at typical velocities >15 km s⁻¹ results in bulk vaporization. It forms a gas phase, induces chemical fractionation, and produces agglutinates (Jolliff et al. 2000; Warren 2008). Limited impact velocities in the laboratory (<7 km s⁻¹) are insufficient to induce significant impact vaporization and measurable chemical fractionation from volatility. Another important conclusion can be drawn from this observation: that ~5 km s⁻¹ impacts of micrometeoroids into the regoliths of Main Belt asteroids likely will not induce chemical fractionation. This in turn suggests that one might readily reconstruct chemical signatures of the impactors from interelement ratios (e.g., Koeberl 1998; Tagle and Hecht 2006; Koeberl et al. 2012; Goderis et al. 2013), which should be preserved in these regoliths (Daly and Schultz 2016, 2018).

CONCLUSIONS

Melting of phonolitic-like glass projectiles occurred during high-velocity impact experiments on a steel target. The impact melt largely covered the craters and was injected into fractures in the crater bottom. Contrary to what is observed in Joule melting experiments where

volatile elements are fractionated with respect to refractory elements, here no fractionation trend is observed. This result contrasts with what is observed for higher energy impact in laser experiments or in some natural impactite samples. Limited impact velocities in the experiments were insufficient to readily induce impact vaporization, especially involving materials like iron and silicate. The absence of measurable chemical fractionation from volatility might also result from the instantaneity of the impact (a few μs), which prevents efficient bulk diffusion of volatile elements in the melt before quenching. The unique chemical modification here is the various Fe contents of the ejecta. They are the result of two processes, i.e., (1) the mechanical removal and mixing of impact melt from the projectile and from the target—a process highly dependent on the energy of impact—and (2) the in situ high-temperature reduction of the impact melt followed by separation of metallic Fe from the silicate impact melt.

In a planetary science perspective, the possible coating of iron asteroid surfaces by micrometeorites can be critical (if significant) for the spectroscopic studies of these bodies: microimpacts may coat the surface with projectile material, preventing trustable conclusions from spectroscopy on the nature of the body. Finally, shock-induced reduction of impact melt should be considered a viable mechanism for the formation of metallic phases.

Acknowledgments—This manuscript benefits from a constructive and detailed review from Christopher Hamann and an anonymous reviewer. The authors thank Olivier Devidal for help in the LA-ICP-MS analyses. We are grateful to S. Hasegawa for technical support related to the experiments using a two-stage light-gas gun at ISAS. Acknowledgment also goes to T. Omura who helped the preparation of the high-speed impact experiments. This research was supported by the Hypervelocity Impact Facility (former facility name: the Space Plasma Laboratory), ISAS, JAXA, Japan. C. G. acknowledges support from PNP-INSU program from the CNRS, and CSI—from the Université de Nice Sophia Antipolis. P. M. and G. L. acknowledge support from the French space agency CNES.

Editorial Handling—Dr. Christian Koeberl

REFERENCES

- Ahrens T. J., Holland K. G., and Chen G. Q. 1998. Shock temperatures and the melting point of iron. *AIP Conference Proceedings* 429:133–136.
- Asimow P. D. and Ghiorso M. S. 1998. Algorithmic modifications extending MELTS to calculate subsolidus phase relations. *American Mineralogist* 83:1127–1131.
- Bottke W. F., Nolan M. C., Greenberg R., and Kolvoord R. A. 1994. Velocity distributions among colliding asteroids. *Icarus* 107:255–268.
- Daly R. T. and Schultz P. H. 2016. Delivering a projectile component to the vestan regolith. *Icarus* 264:9–19.
- Daly R. T. and Schultz P. H. 2018. Projectile preservation during oblique hypervelocity impacts (abstract #1573). 49th Lunar and Planetary Science Conference. CD-ROM.
- Ebert M., Hecht L., Deutsch A., and Kenkmann T. 2011. MEMIN: Chemical modification of projectile spheres, target melts and shocked quartz in hypervelocity impact experiments (abstract #1400). 42nd Lunar and Planetary Science Conference. CD-ROM.
- Ebert M., Hecht L., Deutsch A., and Kenkmann T. 2013. Chemical modification of projectile residues and target material in a MEMIN cratering experiment. *Meteoritics & Planetary Science* 48:134–149.
- Ebert M., Hecht L., Deutsch A., Kenkmann T., Wirth R., and Berndt J. 2014. Geochemical processes between steel projectiles and silica-rich targets in hypervelocity impact experiments. *Geochimica et Cosmochimica Acta* 133:257–279.
- Ebert M., Hecht L., Hamann C., and Luther R. 2017. Laser-induced melting experiments: Simulation of short-term high-temperature impact processes. *Meteoritics & Planetary Science* 52:1475–1494.
- Eisenhüttenleute V. D. and Allibert M. 1995. *Slag atlas*. Düsseldorf, Germany: Verlag Stahleisen.
- Evans N. J., Shahinpoor M., and Ahrens T. J. 1992. Hypervelocity impact: Ejecta velocity, angle, and composition. *Geological Society of America Special Papers* 293:93–102.
- Floss C., El Goresy A., Zinner E., Kransel G., Rammensee W., and Palme H. 1996. Elemental and isotopic fractionations produced through evaporation of the Allende CV chondrite: Implications for the origin of HAL-type hibonite inclusions. *Geochimica et Cosmochimica Acta* 60:1975–1997.
- French B. M. 1998. *Traces of catastrophe: A handbook of shock-metamorphic effects in terrestrial meteorite impact structures*. Houston, Texas: Lunar and Planetary Institute.
- Gerasimov M. V., Yakovlev O. I., Dikov Y. P., and Wlotzka F. 2005. Evaporative differentiation of impact-produced melts: Laser-simulation experiments and comparison with impact glasses from the Logoisk crater. *Geological Society of America Special Papers* 384:351–366.
- Ghiorso M. S. and Sack R. O. 1995. Chemical mass transfer in magmatic processes. IV. A revised and internally consistent thermodynamic model for the interpolation and extrapolation of liquid-solid equilibria in magmatic systems at elevated temperatures and pressures. *Contributions to Mineralogy and Petrology* 119:197–212.
- Gibbons R. V., Hörz F., and Schaal R. B. 1976. The chemistry of some individual lunar soil agglutinates. Proceedings, 7th Lunar and Planetary Science Conference. pp. 405–422.
- Goderis S., Tagle R., Belza J., Smit J., Montanari A., Vanhaecke F., Erzinger J., and Claeys P. 2013. Reevaluation of siderophile element abundances and ratios across the Cretaceous–Paleogene (K–Pg) boundary: Implications for the nature of the projectile. *Geochimica et Cosmochimica Acta* 120:417–446.
- Govindaraju K. and Mevelle G. 1987. Fully automated dissolution and separation methods for inductively coupled plasma atomic emission spectrometry rock analysis. Application to the determination of rare earth elements.

- Plenary lecture. *Journal of Analytical Atomic Spectrometry* 2:615–621.
- Greenstreet S., Gladman B., and McKinnon W. B. 2015. Impact and cratering rates onto Pluto. *Icarus* 258:267–288.
- Güttler C., Blum J., Zsom A., Ormel C. W., and Dullemond C. P. 2010. The outcome of protoplanetary dust growth: Pebbles, boulders, or planetesimals?-I. Mapping the zoo of laboratory collision experiments. *Astronomy & Astrophysics* 513:A56.
- Hamann C., Hecht L., Ebert M., and Wirth R. 2013. Chemical projectile–target interaction and liquid immiscibility in impact glass from the Wabar craters, Saudi Arabia. *Geochimica et Cosmochimica Acta* 121:291–310.
- Hamann C., Stöffler D., and Reimold W. U. 2016a. Interaction of aluminum projectiles with quartz sand in impact experiments: Formation of khatyrkite (CuAl₂) and reduction of SiO₂ to Si. *Geochimica et Cosmochimica Acta* 192:295–317.
- Hamann C., Luther R., Ebert M., Hecht L., Deutsch A., Wünnemann K., Schäffer S., Osterholz J., and Lexow B. 2016b. Correlating laser-generated melts with impact-generated melts: An integrated thermodynamic-petrologic approach. *Geophysical Research Letters* 43.
- Hamann C., Fazio A., Ebert M., Hecht L., Wirth R., Folco L., Deutsch A., and Reimold W. U. 2017. Silicate liquid immiscibility in impact melts. *Meteoritics & Planetary Science*. <https://doi.org/10.1111/maps.12907>
- Horz F., Blanchard D. P., See T. H., and Murali A. V. 1989. Heterogeneous dissemination of projectile materials in the impact melts from Wabar crater, Saudi Arabia. Proceedings, 19th Lunar and Planetary Science Conference. pp. 697–709.
- Jolliff B. L., Gillis J. J., Haskin L. A., Korotev R. L., and Wiczorek M. A. 2000. Major lunar crustal terranes: Surface expressions and crust-mantle origins. *Journal of Geophysical Research: Planets* 105:4197–4216.
- Jutzi M., Holsapple K. H., Wünnemann K., and Michel P. 2015. Modeling asteroid collisions and impact processes. In *Asteroids IV*, edited by Michel P., DeMeo F., and Bottke W. F. Tucson, Arizona: The University of Arizona Press. pp. 679–699.
- Kawai N., Tsurui K., Hasegawa S., and Sato E. 2010. Single microparticle launching method using two-stage light-gas gun for simulating hypervelocity impacts of micro-meteoroids and space debris. *Review of Scientific Instruments* 81:115105.
- Kelly W. R., Holdsworth E., and Moore C. B. 1974. The chemical composition of metallic spheroids and metallic particles within impactite from Barringer Meteorite Crater, Arizona. *Geochimica et Cosmochimica Acta* 38:533–543.
- Koeberl C. 1998. Identification of meteoritic components in impactites. *Geological Society, London, Special Publications* 140:133–153.
- Koeberl C., Claeys P., Hecht L., and McDonald I. 2012. Geochemistry of impactites. *Elements* 8:37–42.
- Kumar P. S. and Kring D. A. 2008. Impact fracturing and structural modification of sedimentary rocks at Meteor Crater, Arizona. *Journal of Geophysical Research: Planets* 113. <https://doi.org/10.1029/2008je003115>
- Le Feuvre M. and Wiczorek M. A. 2011. Nonuniform cratering of the Moon and a revised crater chronology of the inner solar system. *Icarus* 214:1–20.
- Lodders K. 2003. Solar system abundances and condensation temperatures of the elements. *The Astrophysical Journal* 591:1220.
- Lukanin O. A. and Kadik A. A. 2007. Decompression mechanism of ferric iron reduction in tektite melts during their formation in the impact process. *Geochemistry International* 45:857–881.
- Melosh H. J. 1989. *Impact cratering: A geologic process*. Research supported by NASA. New York: Oxford University Press. 253 p.
- Melosh H. J. and Collins G. S. 2005. Planetary science: Meteor Crater formed by low-velocity impact. *Nature* 434:157.
- Mittlefehldt D. W., See T. H., and Hörz F. 1992. Dissemination and fractionation of projectile materials in the impact melts from Wabar Crater, Saudi Arabia. *Meteoritics* 27:361–370.
- Mittlefehldt D. W., Hörz F., See T. H., Scott E. R., and Mertzman S. A. 2005. Geochemistry of target rocks, impact-melt particles, and metallic spherules from Meteor Crater, Arizona: Empirical evidence on the impact process. *Geological Society of America Special Papers* 384:367–390.
- Oberst J., Christou A., Suggs R., Moser D., Daubar I. J., McEwen A. S., Burchell M., Kawamura T., Hiesinger H., Wünnemann K., Wagner R., and Robinson M. S. 2012. The present-day flux of large meteoroids on the lunar surface—A synthesis of models and observational techniques. *Planetary and Space Science* 74:179–193.
- Rowan L. R. and Ahrens T. J. 1994. Observations of impact-induced melted metal-silicate partitioning. *Earth and Planetary Science Letters* 122:71–88.
- Tagle R. and Hecht L. 2006. Geochemical identification of projectiles in impact rocks. *Meteoritics & Planetary Science* 41:1721–1735.
- Walsh K. J., Morbidelli A., Raymond S. N., O'Brien D. P., and Mandell A. M. 2011. A low mass for Mars from Jupiter's early gas-driven migration. *Nature* 475:206–209.
- Warren P. H. 2008. Lunar rock-rain: Diverse silicate impact-vapor condensates in an Apollo-14 regolith breccia. *Geochimica et Cosmochimica Acta* 72:3562–3585.
- Wozniakiewicz P. J., Ishii H. A., Kearsley A. T., Burchell M. J., Bland P. A., Bradley J. P., Dai Z., Teslich N., Collins G. S., Cole M. J., and Russell S. S. 2011. Investigation of iron sulfide impact crater residues: A combined analysis by scanning and transmission electron microscopy. *Meteoritics & Planetary Science* 46:1007–1024.

SUPPORTING INFORMATION

Additional supporting information may be found in the online version of this article.

Fig. S1: Phonolitic beads used as projectile and carbon crucible used for their preparation.

Fig. S2: EDX-chemical map of Fe intensities of an Al-ejecta catcher of experiment n0.

Fig. S3: EDX-chemical map of Si intensities of an Al-ejecta catcher of experiment n0.

Fig. S4: EDX-chemical map of Mg intensities of an Al-ejecta catcher of experiment n0.